

# Initiations of Mesoscale Convective Systems in the Middle Reaches of the Yangtze River Basin Based on FY-4A Satellite Data: Statistical Characteristics and Environmental Conditions

Yanan Fu<sup>1</sup>, Jianhua Sun<sup>2</sup>, Shenming Fu<sup>3</sup>, Yuanchun Zhang<sup>2</sup>, and Zheng Ma<sup>4</sup>

<sup>1</sup>Institute of Atmospheric Physics, Chinese Academy of Sciences

<sup>2</sup>Institute of Atmospheric Physics, Chinese Academy of Sciences

<sup>3</sup>Institute of atmospheric physics, Chinese Academy of Sciences

<sup>4</sup>Institute of Atmospheric Physics, Chinese Academy of Sciences; Cooperative Institute for Meteorological Satellite Studies, University of Wisconsin-Madison, University of Chinese Academy of Sciences

June 13, 2023

# **Initiations of Mesoscale Convective Systems in the Middle Reaches of the Yangtze River Basin Based on FY-4A Satellite Data: Statistical Characteristics and Environmental Conditions**

**Yanan Fu <sup>1,2</sup>, Jianhua Sun <sup>1,2,3</sup>, Shenming Fu <sup>4</sup>, Yuanchun Zhang <sup>1</sup>,  
Zheng Ma <sup>1</sup>**

<sup>1</sup> Key Laboratory of Cloud-Precipitation Physics and Severe Storms, Institute of Atmospheric Physics, Chinese Academy of Sciences, Beijing, China

<sup>2</sup> University of Chinese Academy of Sciences, Beijing, China

<sup>3</sup> Collaborative Innovation Center on Forecast and Evaluation of Meteorological Disasters, Nanjing University of Information Science and Technology, Nanjing, Jiangsu Province, China

<sup>4</sup> International Center for Climate and Environment Sciences, Institute of Atmospheric Physics, Chinese Academy of Sciences, Beijing, China

Corresponding author: Dr. Jianhua Sun ([sjh@mail.iap.ac.cn](mailto:sjh@mail.iap.ac.cn))

## **Key Points**

- The initiations of mesoscale convective systems are backward tracked through a hybrid method of areal overlapping and optical flow
- Quasistationary and outward-moving mesoscale convective systems show notable differences in initiation and developments
- A synoptic circulation pattern associated with the Mei-yu front is most favorable for the initiation of mesoscale convective systems

## 22    **Abstract**

23    Based on the brightness temperature observed by the Fengyun-4A satellite, eight  
 24    hundred mesoscale convective systems (MCSs) are identified in the middle reaches of  
 25    the Yangtze River Basin during the warm seasons (April–September) of 2018–2021,  
 26    and these MCSs are categorized into the quasistationary (QS) type and the  
 27    outward-moving (OM; i.e., moving beyond the source region) type. Afterwards, the  
 28    initiations of the MCSs are backward tracked using a hybrid method of areal  
 29    overlapping and optical flow. Then, the main features of QS and OM MCSs and their  
 30    respective synoptic circulations and environmental parameters are analyzed. The QS  
 31    MCSs primarily occur in July and August and are mainly initiated in the afternoon. The  
 32    OM MCSs mostly occur in June and July with two initiation peaks appeared at noon  
 33    and late night, respectively. The QS MCSs are mainly initiated in mountainous areas. In  
 34    contrast, the OM MCSs are mainly initiated in plain areas. Compared to the OM MCSs,  
 35    the QS MCSs show notable diurnal variation in intensity and develop more rapidly.  
 36    Circulations of a total of 285 days (without direct influences from tropical cyclones) are  
 37    objectively classified into three patterns by using the k-means algorithm. Pattern-I (128  
 38    days), which is closely related to low-level jets, shows the most similar features to those  
 39    of typical Mei-yu fronts, and it acts as the most favorable circulation type for MCS  
 40    initiations. Pattern-II (66 days) is dominated by northwesterlies, with a relatively stable  
 41    layer in the low-level troposphere. Pattern-III (91 days) features a dry-adiabatic or even  
 42    a superadiabatic layer that contributes to decreasing the layer stability.

## 43    **Plain Language Summary**

44    Mesoscale convective systems (MCSs) often cause severe convective weather over  
 45    the middle reaches of the Yangtze River Basin and pose a great threat to life and  
 46    property in this region. This study identified and tracked MCSs using satellite data  
 47    and categorized them into the quasistationary (QS) type and the outward-moving (OM)  
 48    type based on their movement features. The QS type primarily occurs in July and  
 49    August and is mainly initiated in the afternoon over mountains. The OM type mostly  
 50    occurs in June and July and is mainly initiated at noon and late night over the plains.  
 51    Compared to the OM MCSs, the QS MCSs show notable diurnal variation in intensity  
 52    and develop more rapidly. Large-scale circulation regulates environmental conditions  
 53    and further affects the initiation of MCSs. Circulations over the middle reaches of the

Yangtze River Basin are classified into three patterns, each of which is dominated by a large-scale weather system. The circulation pattern dominated by the Mei-yu front is the most favorable for MCS initiation. The circulation pattern dominated by the northwesterly is favorable for the initiation of OM MCSs but not for QS MCSs. The circulation pattern dominated by the southerly produces a strong thermal effect and is favorable for the initiation of QS MCSs.

## 1 Introduction

Severe convective weather phenomena, such as heavy rainfall, hailstorms, wind gusts and tornadoes, are mainly associated with mesoscale convective systems (MCSs) (Houze, 2004; Maddox, 1980; Zheng et al., 2013). The generalized concept of the MCS usually covers broad temporal and spatial scales (Yang et al., 2015), and MCSs exhibit different forms if different techniques of detection and identification are employed. In conventional weather maps, MCSs are generally presented as mesoscale high/low pressures (Zipser, 1977). Based on precipitation observations, MCSs often appear as mesoscale rain clusters or belts (Shen et al., 2020). However, MCSs usually appear as different radar reflectivity morphologies (Gallus et al., 2008; Ma et al., 2021a; Yang & Sun, 2018). On satellite infrared images, MCSs often appear as cold-cloud shields (CCSs) with a certain temporal and spatial scale (Laing & Fritsch, 1997; Machado et al., 1998; Meng et al., 2021; Yang et al., 2015; Zheng et al., 2008).

Using the criteria of brightness temperature and cloud area, Maddox (1980) detected a kind of meso- $\alpha$  scale convective system, which was later known as the mesoscale convective complex (MCC), and since then, the method based on the criteria of brightness temperature and cloud area has been widely used in research on MCCs (Laing & Fritsch, 1997; Miller & Fritsch, 1991; Rodgers et al., 1983; Velasco & Fritsch, 1987). Augustine and Howard (1988) simplified the method of Maddox (1980) and found that applying the criteria of brightness temperature  $\leq -52$  °C and cloud area  $\geq 5 \times 10^4$  km<sup>2</sup> could better describe the evolution of storms. In recent years,  $-52$  °C has been used as the brightness temperature criterion to identify MCSs (Kukulies et al., 2021; Morake et al., 2021; Yang et al., 2015; Yang R. et al., 2020; Meng et al., 2021), and different cloud area and duration criteria have been applied to determine the spatial and temporal scales of MCSs.

Williams and Houze (1987) developed an algorithm to track an individual cloud

86 cluster in two successive infrared images by calculating the overlapping rate of the two  
87 cloud areas, and since then, the areal overlapping method has been widely used in MCS  
88 tracking. Morel and Senesi (2002) improved the accuracy of MCS tracking by  
89 estimating the movement of clouds and developed the ISIS (satellite imagery tracking  
90 instrument) algorithm. Feng et al. (2018) improved the tracking accuracy by expanding  
91 the area of the target cloud and developed the FLEXTRKR (flexible object tracker)  
92 algorithm. In addition, the optical flow approach has been widely used since it was  
93 introduced into meteorology research, including the nowcasting of precipitation  
94 (Bowler et al., 2004; Bechini & Chandrasekar, 2017) and the improvement of  
95 numerical forecast results (Marzban & Sandgathe, 2010). In recent years, the optical  
96 flow approach has been applied in the research of new generation geostationary  
97 satellite products. Vandal and Nemani (2020) improved the temporal resolution of 10.8  
98  $\mu\text{m}$  infrared longwave radiation products of the new generation Geostationary  
99 Operational Environmental Satellite from 15 min to 1 min using the optical flow  
100 approach, and they successfully captured the evolution of a severe convective event.  
101 Burton et al. (2022) applied the optical flow approach to satellite-retrieved rainfall rate  
102 products for West Africa, and extrapolations showed useful skill at up to 4 h of lead  
103 time. In the present study, the areal overlapping method is used to track MCSs, and the  
104 optical flow is calculated to help improve accuracy.

105 Previous studies have mainly focused on the process from the formation to the  
106 termination of an MCS. Due to the data resolution and technical method limitations,  
107 few studies have focused on the initiation of an MCS. Roberts and Rutledge (2003)  
108 suggested that the precursor signal of convection initiation (CI) can be captured on  
109 satellites. Subsequently, two algorithms for identifying precursor signals and predicting  
110 CI based on satellite observations were developed, namely, the SATCAST (satellite  
111 convection analysis and tracking algorithm) algorithm (Mecikalski & Bedka, 2006) and  
112 the UWCI (University of Wisconsin Convective Initiation) algorithm (Sieglaff et al.,  
113 2011). Both scientific research and operational practice have shown that the initiation  
114 of MCSs can be identified through satellite observations.

115 As mentioned above, MCSs have a wide spectrum of spatial and temporal scales,  
116 and the features of MCSs, such as the cloud extent, cloud top temperature and cloud  
117 motion, vary worldwide (Feng et al., 2019; Kolios & Feidas, 2010; Morel & Senesi,  
118 2002; Punkka & Bister, 2015; Rehbein et al., 2018). The activities of MCSs in China

119 have regional characteristics: the highest frequency of MCSs over the Tibetan Plateau  
 120 occurs in July (Zhang et al., 2021; Jiang & Fan, 2002; Mai et al., 2020) and formed  
 121 mainly in the afternoon (Zheng et al., 2008); the activities of MCSs in the North China  
 122 Plain are the most frequent in June, July and August, and the formations occur mostly  
 123 around noon (Ma et al., 2021a); under the influence of sea–land breeze, the MCSs in  
 124 South China propagate offshore (inland) at night (in the daytime) (Bai et al., 2020;  
 125 Zheng et al., 2008).

126 The initiation, development, and organization of MCSs are controlled and  
 127 regulated by synoptic and mesoscale circulations. Lewis and Gray (2010) found that  
 128 MCSs in Britain are mainly affected by three types of circulations and that the  
 129 organization of MCSs is related to the interaction of perturbations at the upper level and  
 130 warm advections at the lower level. Peters and Schumacher (2014) divided the  
 131 circulations favorable for MCSs in the Great Plains of the United States into warm  
 132 season-type and synoptic-type circulations. The synoptic-type MCSs tended to occur  
 133 downstream of a progressive upper-level trough along a low-level potential  
 134 temperature gradient with the warmest air to the south and southeast.  
 135 Warm-season-type MCSs typically occurred within the right-entrance of a minimally to  
 136 anticyclonically curved upper-level jet along a low-level potential temperature gradient  
 137 with the warmest air to the southwest. Song et al. (2019) found that the favorable  
 138 environments for MCSs over the Great Plains of the United States have frontal  
 139 characteristics and enhanced low-level jets, while the unfavorable environments feature  
 140 enhanced upper-level ridges. Sugimoto and Ueno (2010) found that MCSs over the  
 141 eastern Tibetan Plateau mainly occurred under the condition of the eastward extension  
 142 of the upper tropospheric anticyclone with the enhancement of near-surface low  
 143 pressure in the western plateau. He et al. (2017) classified the circulation patterns over  
 144 central East China into nine typical types based on the geopotential height fields at 850  
 145 hPa, and MCSs mainly occurred in the meridional circulations, which were associated  
 146 with the Western North Pacific Subtropical High to the east and a low-pressure system  
 147 to the west. Maurer et al. (2017) identified one particular MCS initiation in the Sahel  
 148 that large-scale convergence forces smaller convective cells initiated at multiple  
 149 locations merging into one larger MCS.

150 Diurnal variations in appearance frequency of the cloud clusters have been found  
 151 over different regions of East Asia (Akiyama, 1989; Asai et al., 1998; Kato et al., 1995;

Li et al., 2007; Takeda & Iwasaki, 1987). Takeda & Iwasaki (1987) found that mesoscale cloud clusters (i.e., MCSs in our study) observed over the ocean tend to form frequently from midnight to early morning, whereas mesoscale cloud clusters over the continent tend to form from afternoon to evening, which might be associated with the difference between radiative processes over the continent and those over the ocean. Akiyama (1989) found that mesoscale cloud clusters tend to develop in the basin areas (in the high-altitude regions) in the morning (in the afternoon), suggesting that the condition of the underlying surface not only causes the different diurnal variations over the continent and the ocean, but also over basin areas and mountainous areas, as we also found in the current study.

The aforementioned studies show that different synoptic circulations often lead to different environmental conditions, and the interactions of environmental conditions, topography, underlying surface and other factors are highly nonlinear, which makes it difficult to forecast the initiation and development of MCSs. Previous studies involving the MCS life cycle are still limited in terms of understanding its formation. At present, thanks to high spatial-temporal resolution satellite data, the development of an MCS from initiation to formation can be accurately captured through backward tracking. The middle reaches of the Yangtze River Basin (YRB) are located in the transitional zone between the second-step terrain (mountains) and the plains over East China, with complicated orography and various underlying surfaces. The Mei-yu fronts are very active in this area, and their precipitation and convection have unique characteristics and complicated mechanisms (Fu et al., 2011b; Sun & Zhang, 2012; Wang et al., 2021; Zhang et al., 2014; Zhang et al., 2020). In the present study, the MCSs over the middle reaches of the YRB are identified and tracked first, and then, the MCS initiation is detected through backward tracking. Next, the temporal-spatial distribution and features of the MCSs are investigated. Finally, the synoptic circulations in this region are objectively classified into different patterns to find the circulations and environmental conditions favorable for the initiation of an MCS. The remainder of this paper is organized as follows. Section 2 introduces the data and methodologies. Section 3 presents the statistics of MCSs, including the temporal-spatial distributions of initiation and apparent features during their life cycles. Section 4 presents the objective classification of circulations in the middle reaches of the YRB and examines the circulation patterns and environmental conditions favorable for MCS initiation.

185 Finally, a summary is given in Section 5.

## 186 **2 Data and methodology**

### 187 **2.1 Data and focus area**

188 The brightness temperature (BT) at the 10.8  $\mu\text{m}$  band of the Advanced  
 189 Geosynchronous Radiation Imager onboard the Fengyun-4A (FY-4A) satellite is used  
 190 to identify and track MCSs in the present study. The spatial resolution of FY-4A BT  
 191 data is 4 km at nadir. The temporal resolution of regional observations over China and  
 192 its surrounding area is  $\sim 5$  min (Yang et al., 2017). The BT fields used in the present  
 193 study are limited to the region ( $\sim 15\text{--}45^\circ\text{N}$  and  $75\text{--}135^\circ\text{E}$ ) shown in Fig. 1a to ensure  
 194 consistency in the dataset. The integrities of the dataset during the warm season (April–  
 195 September) of 2018–2021 are 93.26%, 97.65%, 97.07%, and 98.05%, respectively,  
 196 with an average integrity of 94.51%.

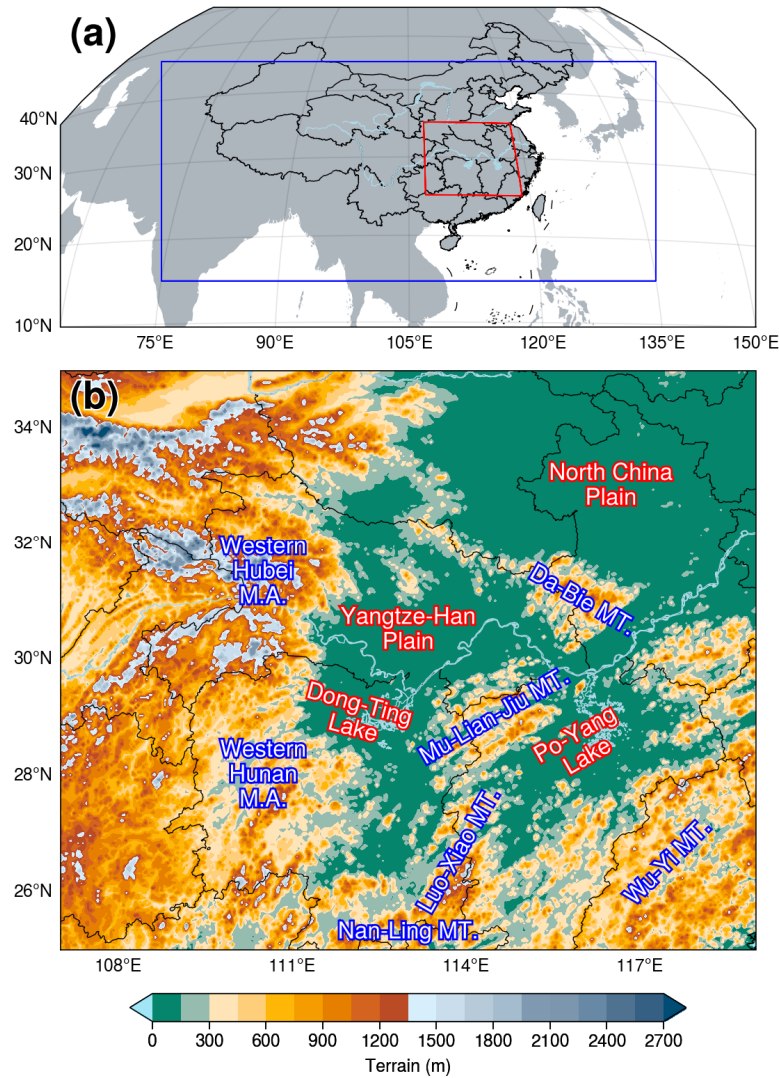
197 Considering that the mechanisms of the convection related to tropical cyclones  
 198 (TCs) are different from those of extratropical convection (Bister, 2001; Hendricks &  
 199 Montgomery, 2006; Rodgers et al., 1991), MCSs induced by TCs and circulations  
 200 related to TCs are excluded using the TC best-track dataset provided by the China  
 201 Meteorological Administration, and the temporal resolution is 3 h (Lu et al., 2021; Ying  
 202 et al., 2014).

203 The fifth-generation ECMWF (European Centre for Medium Range Forecasts)  
 204 reanalysis (ERA5) data, with a temporal resolution of 1 h and a spatial resolution of  
 205  $0.25^\circ$  (Hersbach et al., 2020), are used in the classification and composite analysis of  
 206 circulations. The construction of proximity soundings is mainly based on ERA5 data.  
 207 However, considering the differences in the boundary layer variables between  
 208 reanalysis and observed soundings (Gensini et al., 2014; King & Kennedy, 2019),  
 209 correcting the boundary layer variables of the reanalysis sounding is necessary.  
 210 Therefore, the present study uses the 1-h observations of automatic weather stations  
 211 (AWSs) provided by the China Meteorological Administration to correct the surface  
 212 level of the ERA5 data before constructing proximity soundings.

213 The middle reaches of the YRB are defined as the region covering  $107\text{--}119^\circ\text{E}$  and  
 214  $25\text{--}35^\circ\text{N}$  in the present study (Fig. 1a), and the orography (Fig. 1b) in this area is  
 215 complicated. The western Hubei mountainous areas and western Hunan mountainous



216 areas are located in the west, the Nan-Ling Mountains are in the south and the Wu-Yi  
 217 Mountains are in the southeast. The North China Plain is in the northeastern part of this  
 218 region. Three smaller plains are in the middle, namely, the Jiang-Han Plain, the  
 219 Dong-Ting Lake Plain and the Po-Yang Lake Plain, with the Da-Bie Mountains, the  
 220 Mu-Lian-Jiu Mountains and the Luo-Xiao Mountains distributed from north to south.



221

222 **Figure 1.** (a) The coverage of BT data (blue rectangle) in the present study and the  
 223 boundary of the middle reaches of the YRB (red line). (b) The terrain height (m) in the  
 224 middle reaches of the YRB. Mountains (MT.) and mountain areas (M.A.) are labeled in  
 225 blue, and plains and lakes are labeled in red.

226

## 2.2 Identification and tracking methods

Following Yang R. et al. (2020), the criteria and steps used in the present study to identify MCS are outlined as follows (Fig. 2): 1) detect CCSs with temperature  $\leq -52$  °C and extent  $\geq 5000$  km<sup>2</sup> in the BT fields; 2) track CCSs at different time steps; and 3) continuous CCSs that last longer than 3 h are identified as MCSs. The first (last) time that an MCS satisfies the above criteria is considered to be MCS formation (termination). The time when the CCS of an MCS reaches its maximum extent is considered to be MCS maturity.

The combination of areal overlap and optical flow is used in the present study to track CCSs with the following steps: 1) calculate the optical flow between two successive BT fields; 2) extrapolate the target CCS at the previous time by adding optical flow and compare it with the CCSs at the later time, and the one with an overlapping rate  $\geq 30\%$  is considered the successor of the target CCS; 3) if two CCSs or more satisfy the criterion of the areal overlapping rate at the later time, the one with the highest overlapping rate will be considered the successor of the target CCS; 4) examine the TC locations derived from the best-track dataset, and if there are any TC-related clouds within the coverage of a CCS, the CCS will be excluded because the CCS is a TC cloud instead of an MCS. Backward tracking is applied to find the initiation time and location of an MCS. Considering that the CCS is small and develops rapidly during the early stage of an MCS, no areal limitation has been applied during backward tracking.

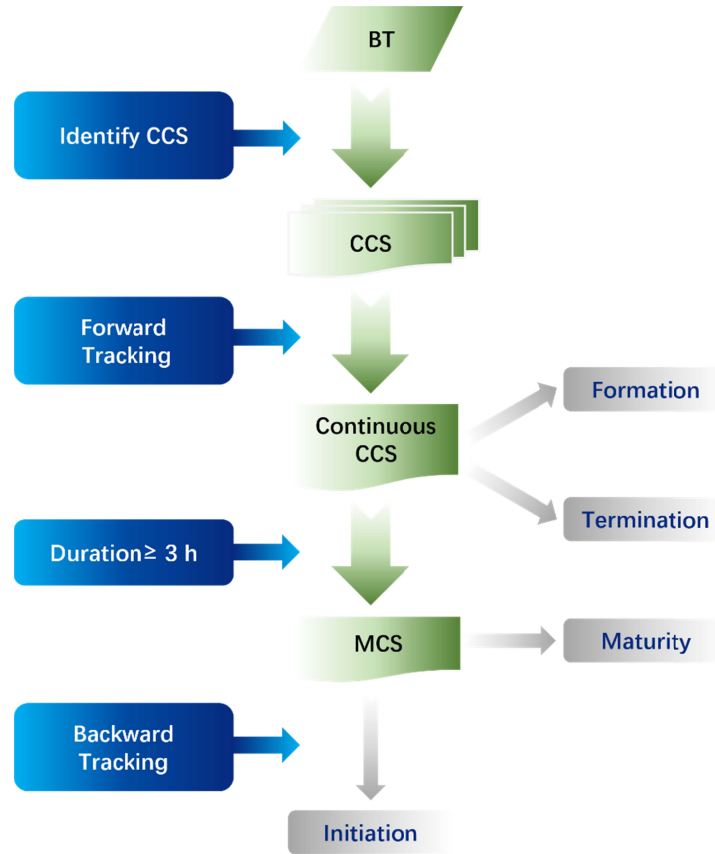


**Figure 2.** Flow chart of MCS identification and tracking.

### 2.3 Filtering of backward tracking

Backward tracking may not be accurate because the extent of a CCS is small and the motion is fast during the early stage of an MCS. The splitting and regeneration of MCSs, cirrus anvils, and deficiency of BT data may all lead to incorrect backward tracking. Therefore, further examinations are conducted on the backward tracking results. If two or more MCSs are initiated at the same time and location, it is considered that those MCSs are split from the same MCS or that one MCS is regenerated from another. Then, the initiation will be assigned to the earliest MCS according to the formation time, and the remaining MCSs will be regarded as inaccurate tracking and excluded from the MCS dataset. For the inaccurate backward tracking results caused by deficiency of BT data, the filtering approach is outlined as follows: check whether the BT data before the initiation time are missing; if true, the result will be regarded as inaccurate and excluded from the MCS dataset. CCSs connected with cirrus anvils are manually checked since they vary greatly between two successive times.

## 2.4 Objective classification

The *k-means* algorithm, which is widely used for classification in atmospheric research due to its stable performance (Hoffmann & Schlünzen, 2013; Huth et al., 2008; Kanungo et al., 2002; Ku et al., 2021; Solman & Menéndez, 2003; Stahl et al., 2006; Zhang et al., 1997), is applied in the present study for the objective classification of circulation patterns. The meteorological variable used for classification in the present study is the geopotential height field at 700 hPa. The geopotential height field is a commonly used variable in circulation classification (Hoffmann & Schlünzen, 2013; Liu et al., 2019; Miao et al., 2017; Ning et al., 2020; Yang et al., 2021). Huth et al. (2008) suggested that due to a high degree of dependence among individual levels, the inclusion of additional levels yields little extra information over using a single level, which has been confirmed in many studies (Dong et al., 2020; Liu et al., 2019; Miao et al., 2017; Ning et al., 2020; Yang et al., 2021). The isobaric layer of 700 hPa is chosen mainly considering that the isobaric layer of 850 hPa and below may be influenced by the topography, of which the average altitude is ~1200 m over the mountainous areas in the middle reaches of the YRB. Statistics (see Section 3) in the present study suggest that MCSs are mainly initiated between 0300–0600 (Coordinated Universal Time, UTC) and that 78.4% (627 out of 800) of MCSs occur in June, July and August (JJA). In addition, circulation patterns vary greatly in September (Tao 1980). Therefore, the geopotential height fields at 700 hPa at 0000 UTC each day during JJA of 2018–2021 are used for circulation classification. TCs may have a great impact on synoptic circulations, leading to inaccurate classification results. Therefore, based on the TC locations derived from best-track data, if a TC enters the area west of 124 °E and north of 20 °N on a certain day, this day will be recorded as a TC-day and will be excluded during circulation classification. A total of 83 TC days are excluded.

The silhouette coefficient (Rousseeuw, 1987) is calculated as an approach to evaluate the performance of different classification numbers. The silhouette coefficient considers both the homogeneity within a class and the difference between classes (Huth

et al., 2008; Rousseeuw, 1987) and is widely used as criterion to determine the classification number (Bernard et al., 2013; Nga et al., 2021; Ternynck et al., 2016). The optimal choice of classification number in the present study is 3 based on the evaluation of the silhouette coefficient.

## 2.5 Construction of proximity soundings

Considering the coarse temporal-spatial resolutions of the observed radiosonde data, the environmental parameters in the present study are calculated from the reanalysis-derived proximity soundings based on ERA5 data. However, some previous studies have noted the differences in the boundary layer variables between reanalysis and observed soundings and that correcting the boundary layer variables of the reanalysis sounding is necessary (Gensini et al., 2014; King & Kennedy, 2019). Therefore, the hourly AWS observations are used to correct surface-level variables in ERA5 data before calculating environmental parameters.

The nearest hour before an MCS initiation and the ERA5 grid closest to the initiation are chosen as the time and location, respectively, to construct a proximity sounding. The closest AWS observation to the ERA5 grid within a radius of 100 km of the grid is selected to correct the surface-level variables of the ERA5 data. The ERA5 temperature/dew-point temperature profile is first constructed based on the isobaric layers (all 37 layers from 1000 hPa to 1 hPa). Then, the isobaric layers below the AWS surface pressure layer are neglected, and the AWS variables are deemed the lowest layer of the proximity sounding (Brooks et al., 2003; Ma et al., 2021b; Yang & Sun, 2018).

The environmental parameters are calculated based on proximity soundings to investigate the dynamic and thermodynamic conditions of MCS initiation under different circulation backgrounds. Ten parameters are selected, namely, the surface-based convective available potential energy (SBCAPE), the most unstable layer convective available potential energy (MUCAPE), surface-based convective inhibition (SBCIN), most unstable layer convective inhibition (SBCIN), lifted index (LI), lifted condensation level (LCL), level of free convection (LFC), precipitable water (PW), 0–3 km bulk wind shear (SHR3) and 0–6 km bulk wind shear (SHR6). These parameters, with clear physical meanings and good performances in distinguishing between different intensities and types of convection, are widely used in convection

environment studies (Brotzge et al., 2013; Grams et al., 2012; J. C. Kirkpatrick et al., 2007; Ma et al., 2021b; McCaul & Weisman, 2001; Yang & Sun, 2018).

### 3 Statistical characteristics

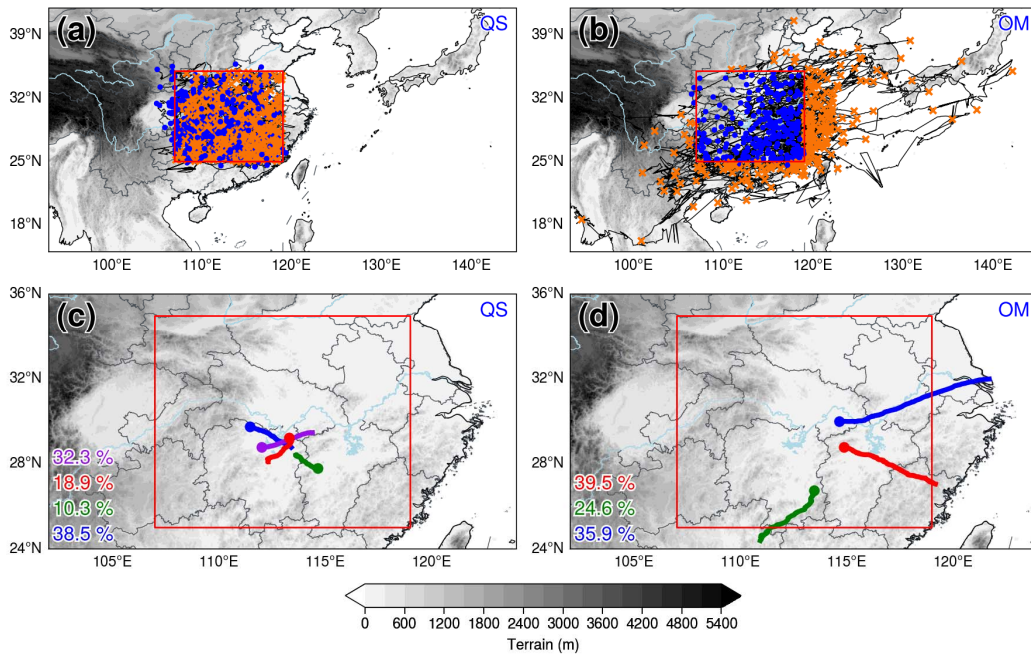
#### 3.1 MCS trajectories and paths

On the one hand, the movements and propagations of MCSs are closely related to the occurrences of convective weather phenomena; on the other hand, they represent the regulation of large-scale circulations over mesoscale systems (Li et al., 2008; Yang J. et al., 2020; Jiang & Fan, 2002; Mai et al., 2020). In the present study, MCSs are categorized into quasistationary (QS) and outward-moving (OM) types. For QS MCSs, both the formations and terminations occur within the study area (Fig. 1b), and OM MCSs refer to those formed within the study area but terminated outside of the study area.

During the warm seasons (April–September) of 2018–2021, 800 MCSs are identified in the middle reaches of the YRB, where 524 are QS type and 276 are OM type, accounting for 65.5% and 34.5% of the total MCSs, respectively. Based on the movement trajectories of the MCSs, those of the QS type (Fig. 3a) are short and mainly within the study area. Part (13.7%) of the QS MCSs moved outside of the study area at certain times during their life cycles; however, they moved back into and terminated within the study area. The trajectories of OM MCSs (Fig. 3b) are longer than those of QS MCSs and are mainly eastward and southward. Most of the OM MCSs terminated after propagating into the oceanic area; however, some OM MCSs with long trajectories could reach the Pacific Ocean east of Japan or north of the Indo-China Peninsula.

To further investigate the main paths of the two types of MCSs, the *k-means* algorithm is adopted to classify MCS trajectories. Based on the evaluation of the silhouette coefficient, the trajectories of QS (OM) MCSs are classified into four (three) kinds of main paths. Among the four kinds of paths of the QS MCSs (Fig. 3c), the number of MCSs in the southeast kind is the largest, and the northwest kind is the smallest. The lengths of the northeast and southeast kinds are long, while those of the northwest and southwest kinds are short. Except for the northwest kind with the smallest number of MCSs, the other three kinds of paths all move from the mountains

to the plains. The phenomenon that convective cells are initiated in mountainous areas and propagate to the plains often occurs in the Rocky Mountains and the Great Plains of the United States (Carbone et al., 2002; Zhang et al., 2014) and the Tai-Hang Mountains and the North China Plain (He & Zhang, 2010; Zhu et al., 2018), which is related to the mountain-plain solenoid driven by thermodynamic effects (Bao et al., 2011; Sun & Zhang, 2012; Zhang & Sun, 2017). For the OM MCSs, among the three kinds of paths (Fig. 3d), the number of MCSs in the southeast kind is the largest. The northeast kind has the longest length, followed by the southeast kind, and the southwest kind has the shortest length.



363

**Figure 3.** The movement trajectories of QS MCSs (a) and OM MCSs (b) and the composite movement paths of QS MCSs (c) and OM MCSs (d). The blue dots (orange crosses) in (a) and (b) represent the initiation (termination) locations of MCSs. Different kind of paths are distinguished by different colors in (c) and (d), and the proportions of trajectories in different kinds are marked in the lower left corner. The gray shading represents terrain height (m). The red rectangle indicates the boundary of the middle reaches of the YRB.

371

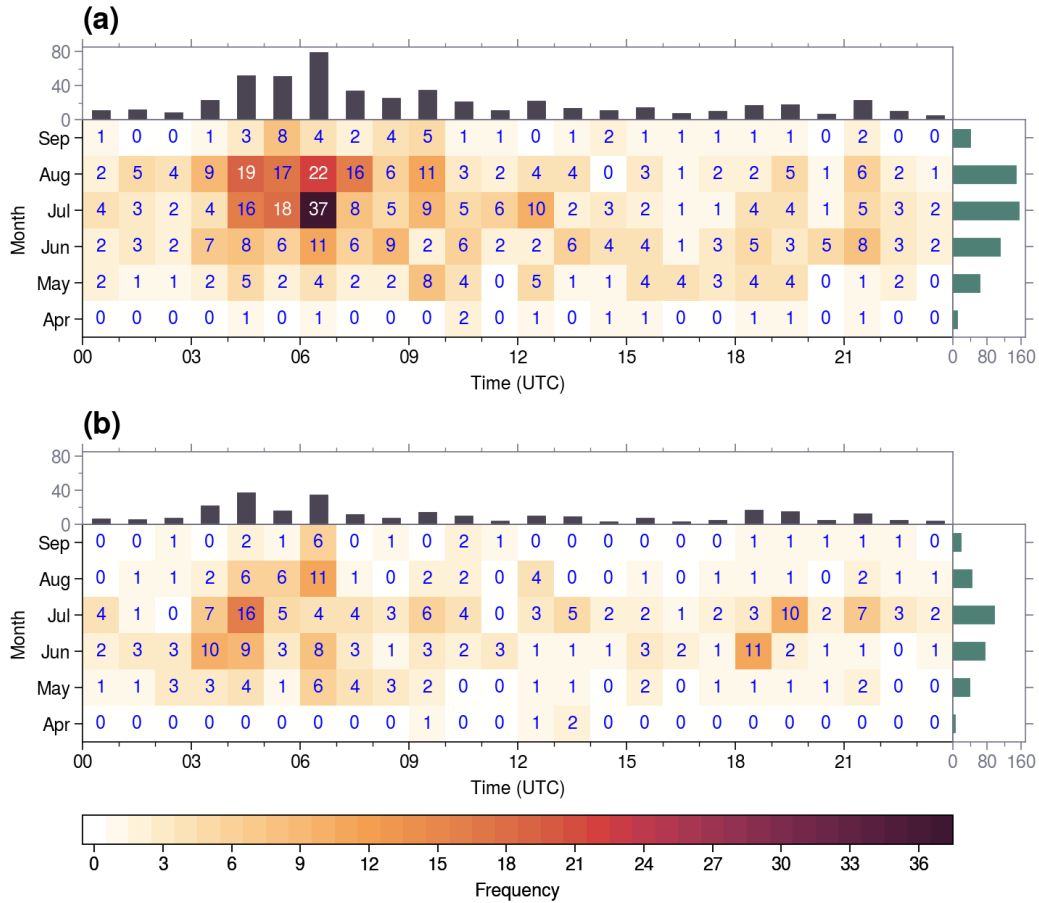
### 3.2 Temporal-spatial distribution of MCS initiations

372

The temporal distributions of MCS initiation are shown in Fig. 4. The QS MCSs

373 mostly occur in July, followed by August (Fig. 4a), while the OM MCSs occur most  
374 frequently in July, followed by June (Fig. 4b). During the Mei-yu season in the YRB,  
375 namely, mid-June to mid-July (Tao, 1980), the mesoscale systems basically move  
376 eastward along the Mei-yu front. After mid-July, the convective cells in this area are  
377 mainly caused by local diabatic effects. These results explain why QS MCSs mostly  
378 occur in July and August, while OM MCSs mostly occur in June and July (Zhang et al.,  
379 2014). The QS MCSs are mainly (41.2%) initiated around noon (0400–0800 UTC), and  
380 the peak time is 0600–0700 UTC, which is identical in each month (Fig. 4a). However,  
381 the peak hours of initiation for OM MCSs vary in different months. In June and July,  
382 the initiation of OM MCSs has two peaks, one at noon (0300–0500 UTC) and the other  
383 at night (1800–1900 UTC). The noon peak is generally considered to be related to the  
384 instability caused by surface solar heating (Yu et al., 2007), and MCSs initiated during  
385 this time period correspond to the afternoon peak of summer precipitation in the YRB  
386 (Luo et al., 2016; Zhang et al., 2020). The mechanism for the late-night peak is  
387 complicated, which may result from instability due to nocturnal radiative cooling at the  
388 cloud top (Lin et al., 2000), water vapor accumulation at low levels in the evening  
389 (Kubota & Nitta, 2001), or diurnal variation in local circulation forced by complex  
390 terrain (He & Zhang, 2010; Li et al., 2005; Sun & Zhang, 2012; Zhang & Sun, 2017).  
391 Regardless of the triggering mechanism, the late-night initiation peak of the OM MCS  
392 corresponds to the morning peak of precipitation in the typical Mei-yu seasons (Luo et  
393 al., 2016; Zhang et al., 2020). In other months (except for September, which has only 4  
394 MCSs), OM MCSs have only one peak in the afternoon (0600–0700 UTC), which is  
395 consistent with the QS type.





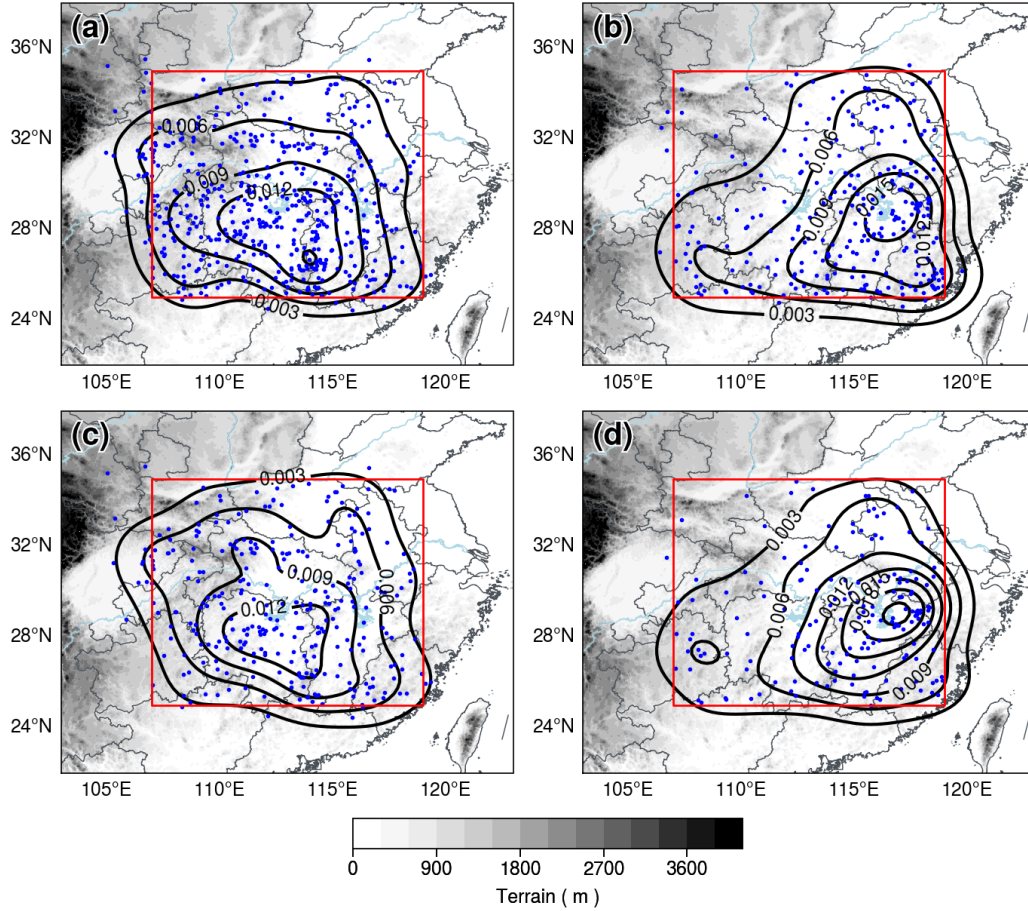
396

397 **Figure 4.** Monthly and diurnal distributions of the QS MCS frequency (a) and the OM  
 398 MCS frequency (b) in the middle reaches of the YRB during the warm seasons (April–  
 399 September) of 2018–2021. The horizontal axis represents the initiation time (UTC).  
 400 The color shading symbolizes the occurrence frequency of MCSs.

401 The spatial distributions of MCS initiation are shown in Fig. 5. Both the QS  
 402 MCSs (Fig. 5a) and the OM MCSs (Fig. 5b) are initiated mainly in the southern part of  
 403 the YRB, which is consistent with a previous study (Zheng et al., 2008). Dividing the  
 404 southern part of the YRB from the north roughly by 30 °N, 343 QS MCSs and 195 OM  
 405 MCSs are initiated in the southern part of the YRB, accounting for 65.5% and 70.7% of  
 406 their total amounts, respectively. The highest initiation frequency of QS MCSs is found  
 407 over the western Hunan Mountains, the Mu-Lian-Jiu Mountains and the Luo-Xiao  
 408 Mountains, while that of the OM MCSs is over the Po-Yang Lake Plain. The  
 409 convection in mountainous areas is mainly driven by the thermodynamic forcing  
 410 (Astling, 1984; Panosetti et al., 2016; Zhu et al., 2018), while in plain areas, due to the

411 lack of dynamic forcing or diabatic heating resulting from the complex terrain, the  
412 initiation of convection is mostly related to synoptic circulation systems (Reif &  
413 Bluestein, 2017; Wilson & Roberts, 2006), which explains why QS MCSs are more  
414 likely to be initiated over mountainous areas, while OM MCSs tend to be initiated over  
415 plain areas.

416       To better illustrate the spatial distributions of MCS initiation, July and August  
417 (June and July) are chosen as the high occurrence period for QS (OM) MCSs. For QS  
418 MCSs, the spatial distribution of initiation in July and August (Fig. 5c) is basically the  
419 same as in the entire warm season (Fig. 5a), and the highest initiation frequency is also  
420 over the western Hunan mountains, the Mu-Lian-Jiu Mountains and the Luo-Xiao  
421 Mountains (Fig. 1b), with the highest probability density of 0.015 (0.014 for the entire  
422 warm season). Although in-depth studies are required, this consistency further indicates  
423 that the initiation of QS MCSs in the middle reaches of the YRB may be caused by local  
424 topographic forced thermal circulation and thus varies little in different months. For the  
425 OM MCSs, the spatial distribution of initiation in June and July (Fig. 5d) exhibits some  
426 differences compared with that of the entire warm season (Fig. 5b). Over the Po-Yang  
427 Lake Plain (Fig. 1b), the maximum probability density increases from 0.017 to 0.022,  
428 indicating that in June and July, OM MCSs are more likely to be initiated over the plain  
429 areas. In addition, the probability density contours extend from the maximum over  
430 Po-Yang Lake to the southwest along the Luo-Xiao Mountains and to the southeast  
431 along the Wu-Yi Mountains (Fig. 1b) in the entire warm season, but in June and July,  
432 the probability density contours show fewer extensions outward from the maximum  
433 center, indicating that the initiation of OM MCSs is less related to the terrain in June  
434 and July.



435

436 **Figure 5.** The spatial distribution of initiation locations of QS MCSs during the entire  
 437 warm season (a) and in July and August (c) and OM MCSs during the entire warm  
 438 season (b) and in June and July (d). The blue dots represent initiation locations, from  
 439 which the spatial probability density is calculated and exhibited by the black contours.  
 440 The red rectangle marks the middle reaches of the YRB. The gray shading represents  
 441 terrain height (m).

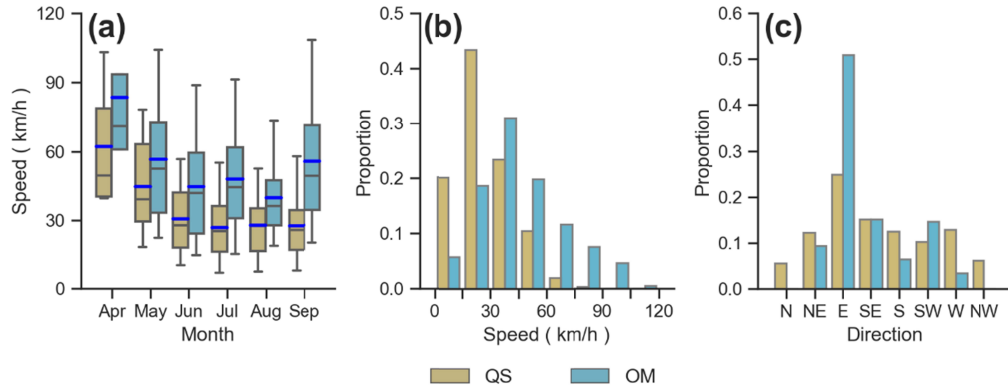
442

### 3.3 Features of MCS movement

443

The moving velocity of an MCS between two consecutive times is calculated  
 444 based on the centroid locations and the time interval. The average moving velocity of  
 445 all times in the entire life cycle of an MCS is considered to be the bulk moving velocity  
 446 of the MCS. In general, the speeds of OM MCSs are faster than those of QS MCSs (Fig.  
 447 6a). The movement of the MCS is regulated by the steering wind in the mid-lower  
 448 troposphere (Rehbein et al., 2018); therefore, both the QS and OM MCSs move faster  
 449 in April and May and slower in June, July and August. The speeds of the QS (OM)

463 MCSs are basically the same in July and August (June and July), indicating that the  
 464 selection of a high occurrence period is reasonable. The speeds and directions of QS  
 465 MCSs and OM MCSs in their high occurrence period are shown in Figs. 6 b and c.  
 466 More than 80% of QS MCSs move at speeds of 0–45 km h<sup>-1</sup>, and the highest proportion  
 467 is located in the range of 15–30 km h<sup>-1</sup>, accounting for 44% of all QS MCSs. Most  
 468 (more than 70%) OM MCSs move at speeds of 15–60 km h<sup>-1</sup>, with the highest  
 469 proportion in the range of 30–45 km h<sup>-1</sup>, accounting for 32%. The moving directions of  
 470 the QS MCSs are relatively evenly distributed in all 8 directions in July and August  
 471 with roughly similar proportions, which also indicates that the QS MCSs in July and  
 472 August are less related to the activities of synoptic systems. The synoptic systems in the  
 473 middle reaches of the YRB generally move eastward (Fu et al., 2011a; Zhang et al.,  
 474 2018; Zhang & Sun, 2017), resulting in more than 50% of OM MCSs moving eastward  
 475 and no OM MCS moving north or northwestward.



464

470 **Figure 6.** Box-and-whisker plot of MCS speed (a, km h<sup>-1</sup>) during the warm seasons of  
 471 2018–2021 (a). The upper and lower edges (caps) of the boxes (whiskers) in the  
 472 box-and-whisker plot represent the 3rd and 1st quartiles (95th and 5th percentiles),  
 473 respectively. The black (blue) dashes inside boxes represent the medians (mean values).  
 474 Histograms of MCS movement speeds (b, km h<sup>-1</sup>) and directions (c) in the high  
 475 occurrence period.

#### 471 3.4 Duration, maximum extent and lowest temperature of MCSs

474 The duration and maximum extent represent the temporal-spatial scale of an  
 475 MCS, and the lowest brightness temperature may reflect the intensity of the strongest  
 476 convection in the MCS. In this section, box-and-whisker plots are applied to examine

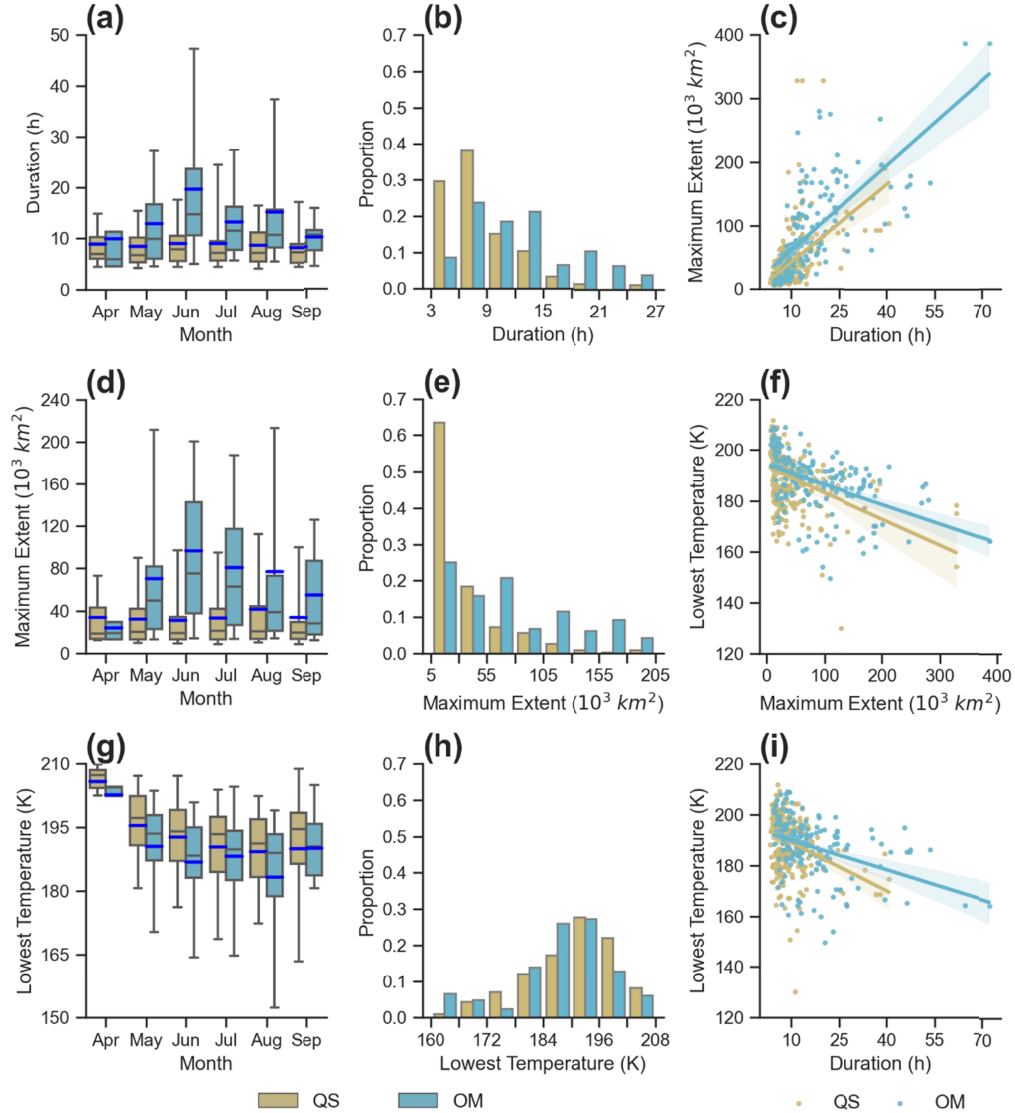
the distributions of the three features in the entire warm season (Figs. 7 a, d and g). Then, the proportion distributions (Figs. 7 b, e and h) and the pairwise relationships (Figs. 7 c, f and i) of these features in the high occurrence period (July and August for the QS MCSs and June and July for the OM MCSs) are analyzed.

Basically, the OM MCSs last longer than the QS MCSs (Fig. 7 a). The QS MCSs mainly last for 5–10 h, with no significant variations between different months. The OM MCSs in June last longer than those in other months, with an average duration of ~20 h. The maximum extents of QS MCSs are mainly smaller than  $5 \times 10^4 \text{ km}^2$ , while those of OM MCSs are mostly between  $2 \times 10^4 \text{ km}^2$  and  $1.5 \times 10^5 \text{ km}^2$  and vary from month to month. The lowest temperature shows a similar distribution between the QS MCSs and the OM MCSs with an average value of approximately 190 K. The mechanisms of initiation and development of QS MCSs may be related to the local topographically forced thermal circulation, resulting in little difference in duration and maximum extent between months. However, OM MCSs are mainly caused by synoptic systems that vary in different months in the middle reaches of the YRB (Wang et al., 2021; Sun et al., 2018), leading to complexity in the mechanisms of the initiation and development of OM MCSs, further resulting in differences in duration and maximum extent between months.

In July and August, nearly 40% of QS MCSs last 6–9 h and 30% last 3–6 h. In June and July, more than 60% of OM MCSs last 6–15 h, with ~20% of each 3-h interval. The maximum extents of QS MCSs in July and August are mainly  $5 \times 10^3$ – $3 \times 10^4 \text{ km}^2$ , accounting for more than 60%, while the maximum extents of the OM MCSs in June and July are distributed evenly in the  $5 \times 10^3$ – $3 \times 10^4 \text{ km}^2$ ,  $3 \times 10^4$ – $5.5 \times 10^4 \text{ km}^2$  and  $5.5 \times 10^4$ – $8 \times 10^4 \text{ km}^2$  intervals, with each accounting for ~20%. For the lowest temperature, half of the QS (OM) MCSs are 184–196 K (190–202 K) in July and August (June and July).

Based on the above analysis, there are certain connections among the duration, maximum extent and lowest temperature of MCSs. The pairwise correlations of the three features in the high occurrence period are shown in Figs. 7 c, f and i. In general, the longer the durations of the MCSs are, the larger the maximum extents and the colder the cloud tops. With the extension of duration, the maximum extent shows an enlarging trend (Fig. 7c), which is consistent between the QS type and the OM type. With the

510 increase in the maximum extent, the lowest temperature decreases (Fig. 7f), and that of  
 511 the QS type decreases faster than that of the OM type. With increasing duration, the  
 512 lowest temperature shows a decreasing trend (Fig. 7i), and that of the QS MCSs also  
 513 decreases faster.



511  
 516 **Figure 7.** The box-and-whisker plots on the left are the duration (a), the maximum  
 517 extent (d) and the lowest temperature (g) of MCSs during the entire warm seasons of  
 518 2018–2021. The upper and lower edges (caps) of the boxes (whiskers) in the  
 519 box-and-whisker plot represent the 3rd and 1st quartiles (95th and 5th percentiles),  
 520 respectively. The black (blue) dashes inside boxes represent the medians (mean values).

The histograms of the central column are the proportion of the duration (b), the maximum extent (e) and the lowest temperature (h) of MCSs in high occurrence periods of 2018–2021. The scatter plots on the right are the pairwise relationships between the duration and the maximum extent (c), the maximum extent and the lowest temperature (f), and the duration and the lowest temperature (i) in high occurrence periods of 2018–2021.

### 3.5 Diurnal variation in maximum extent and lowest temperature

Li et al. (2007) found that occurrence frequency and the intensity of the cloud clusters has diurnal variations. Therefore, to what extent do the QS MCSs and the OM MCSs differ from each other with regard to the diurnal variations in intensity? This question is addressed in this subsection.

To investigate the diurnal variation in the MCSs in the middle reaches of the YRB, the time when the maximum extent (lowest temperature) appears and the time span between MCS initiation and the maximum extent (lowest temperature) appearance are further examined. Since 58% of QS MCSs are initiated in July and August and 62% of OM MCSs occur in June and July, to highlight the difference between QS MCSs and OM MCSs, only MCSs in high occurrence periods are analyzed, and the results are shown in Fig. 8.

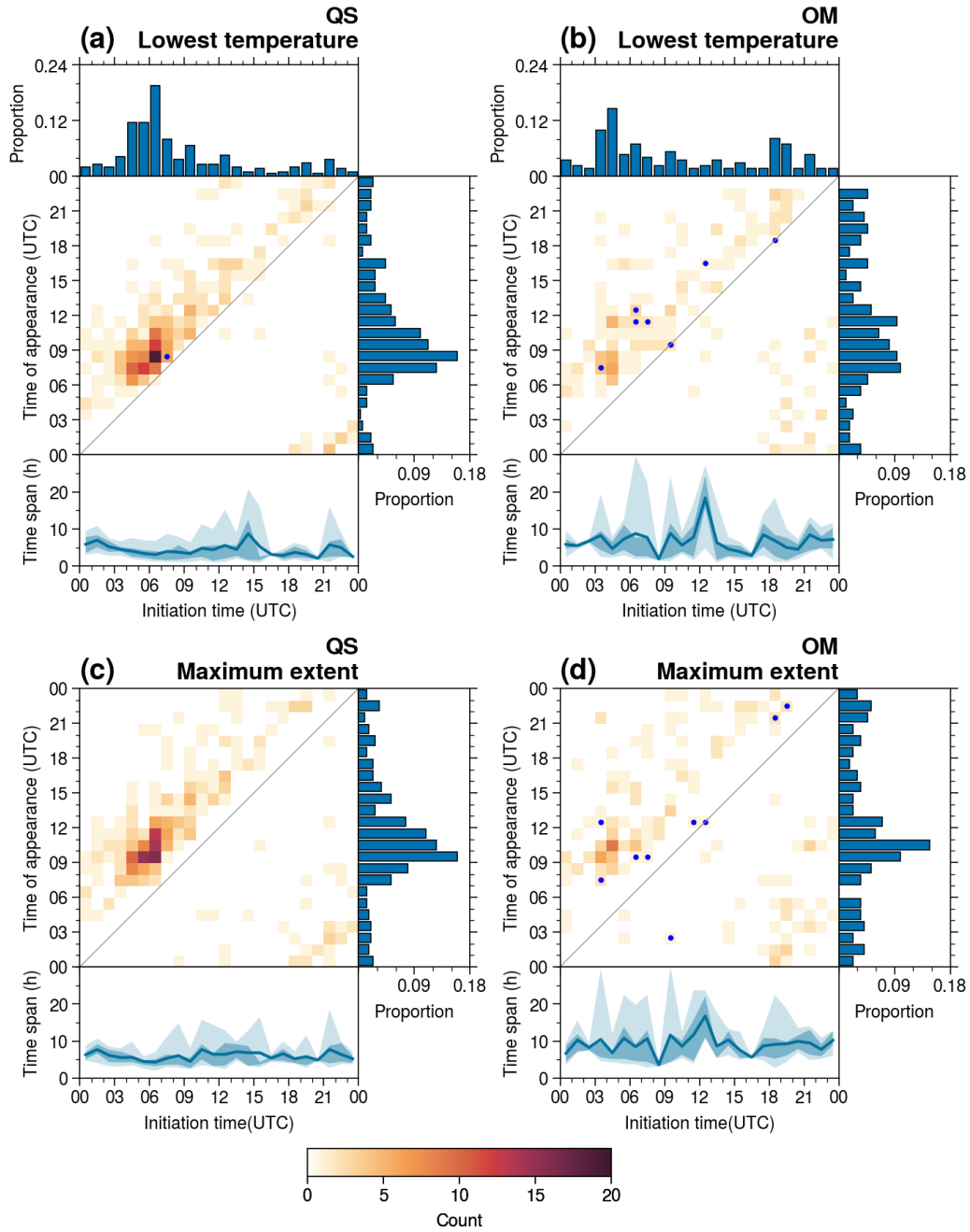
In July and August, the initiation frequency of QS MCSs peaks in the afternoon (0600–0700 UTC, Fig. 8a, upper subplot), which is the same as the result from the entire warm season (Fig. 3a). In June and July, the initiation frequency of OM MCSs has two peaks, namely, noon peak (0300–0500 UTC) and late-night peak (1800–2000 UTC, Fig. 8b, upper subplot). For the OM MCSs, compared with the result from the entire warm season (Fig. 3b), the proportions of MCS initiation during the noon peak (0300–0500 UTC) and the late-night peak (1800–2000 UTC) increase, but that during the afternoon peak (0600–0700 UTC) decreases.

In July and August, the lowest temperatures of QS MCSs mainly appear in the afternoon (0700–1100 UTC), with a peak at 0800–0900 UTC (Fig. 8a, the main plot and the subplot on the right-hand side). The surface solar heating is the strongest in the afternoon; therefore, convective activities are most vigorous during this time period. In June and July, the lowest temperatures of OM MCSs mainly appear in the afternoon

and the evening, distributed evenly during this time period without any obvious peak (Fig. 8b, the main plot and the subplot on the right-hand side). As mentioned before, the mechanisms for convection development in the OM MCSs are complicated, resulting in no obvious peak for the lowest temperature appearance. In July and August, the maximum extents of QS MCSs mainly appear in the evening (0900–1200 UTC, Fig. 8c, the main plot and the subplot on the right-hand side), 1–2 h later than the appearance of the lowest temperature. In June and July, the maximum extents of OM MCSs mainly appear in the evening (0900–1100 UTC) (Fig. 8d, the main plot and the subplot on the right-hand side).

In July and August, the lowest temperatures (the maximum extents) of the QS MCSs appear 4.43 h (6.03 h) after initiation. The QS MCSs initiated at noon or in the afternoon (0500–1000 UTC) reach the lowest temperature ~3 h after initiation (Fig. 8a, lower subplot), which indicates that the QS MCSs initiated in this time period develop at roughly the same pace. The QS MCSs in July and August mainly achieve the maximum extent 4–7 h after initiation (Fig. 8c, lower subplot). In June and July, the lowest temperatures (maximum extents) of the OM MCSs appear 6.8 h (9.21 h) after initiation (lower subplots in Figs. 8 b and d). The development of OM MCSs is associated with many factors (i.e., synoptic systems, orography, and underlying surface) and interactions between these factors; therefore, the diurnal variations follow no obvious pattern.





567

568 **Figure 8.** The two-dimensional histogram for the diurnal variation in the lowest  
 569 temperature appearance of QS MCSs (a) and OM MCSs (b) and the maximum extent  
 570 appearance of QS MCSs (c) and OM MCSs (d) in the high occurrence period of 2018–  
 571 2021. The main body of each plot exhibits the frequency of MCS initiation and the  
 572 lowest temperature (maximum extent) in every hourly interval. The upper histogram  
 573 exhibits the proportion of MCS initiation. The left histogram exhibits the proportion of  
 574 the lowest temperature (maximum extent) appearance. The lower plot exhibits the time

span between the lowest temperature (maximum extent) appearance and MCS initiation, with the solid line representing the mean time span and the light (dark) shading representing the 5%–95% (25%–75%) percentile interval. The blue dot indicates that the time span is longer than 24 h.

#### 4 Circulation patterns and environmental conditions for MCS initiation

To investigate the circulation patterns favorable for MCS initiation, the daily circulations at 0000 UTC in JJA of 2018–2021 are objectively classified into 3 patterns by adopting the *k-means* algorithm, and the environmental parameters under different circulation patterns are further analyzed.

##### 4.1 Objective classification of circulation patterns

Circulations of 285 days without direct influences from tropical cyclones in JJA of 2018–2021 are classified into 3 patterns according to the evaluation based on the silhouette coefficient, with 128, 66 and 91 days in each pattern, respectively, and the composite fields of geopotential height at 700 hPa are shown in Fig. 9.

Pattern-I (P1) is the typical circulation of the Mei-yu front (Fig. 9a). With a shallow trough in northeast China and the Indo-China Peninsula, the middle reaches of the YRB are in a large-scale convergence zone formed by the northwesterly flow from the high latitudes and the southwesterly flow from the low latitudes, which is consistent with the shear line and the strong equivalent potential temperature gradient. In Pattern-II (P2), the middle reaches of the YRB are basically under the control of the northwesterly, to the east of which is a deep trough (Fig. 9b). Although the equivalent potential temperature field also shows a strong gradient in P2, the thermodynamic characteristics of circulations in P1 and P2 are different. In P1, a warm humid air flow is dominated by the strong southwesterly, with a warm tongue extending from southwest to northeast. In P2, the northwesterly is the dominant wind, steering a cold tongue extending from north to south. The equivalent potential temperature field in P1 (336–348 K) is higher than that in P2 (332–340 K), indicating that the air mass in P1 is warmer or moister than that in P2. In Pattern-III (P3), the middle reaches of the YRB are under the control of the weak southerly to the east of the Western Pacific Subtropical High.

Note that although circulations in P1 are related to the Mei-yu front, not all the

MCSs are initiated within the Mei-yu frontal zone. In fact, many MCSs in P1 are initiated in the strong southwesterly flow to the south of the Mei-yu front rather than around the Mei-yu frontal zone. The mechanism for MCS initiations under such synoptic patterns may be related to the cold dome ahead of the Mei-yu front generated by previous convection, which promotes initiation by lifting high equivalent potential temperature air in the southwesterly flow to its level of free convection (Luo & Chen, 2015).

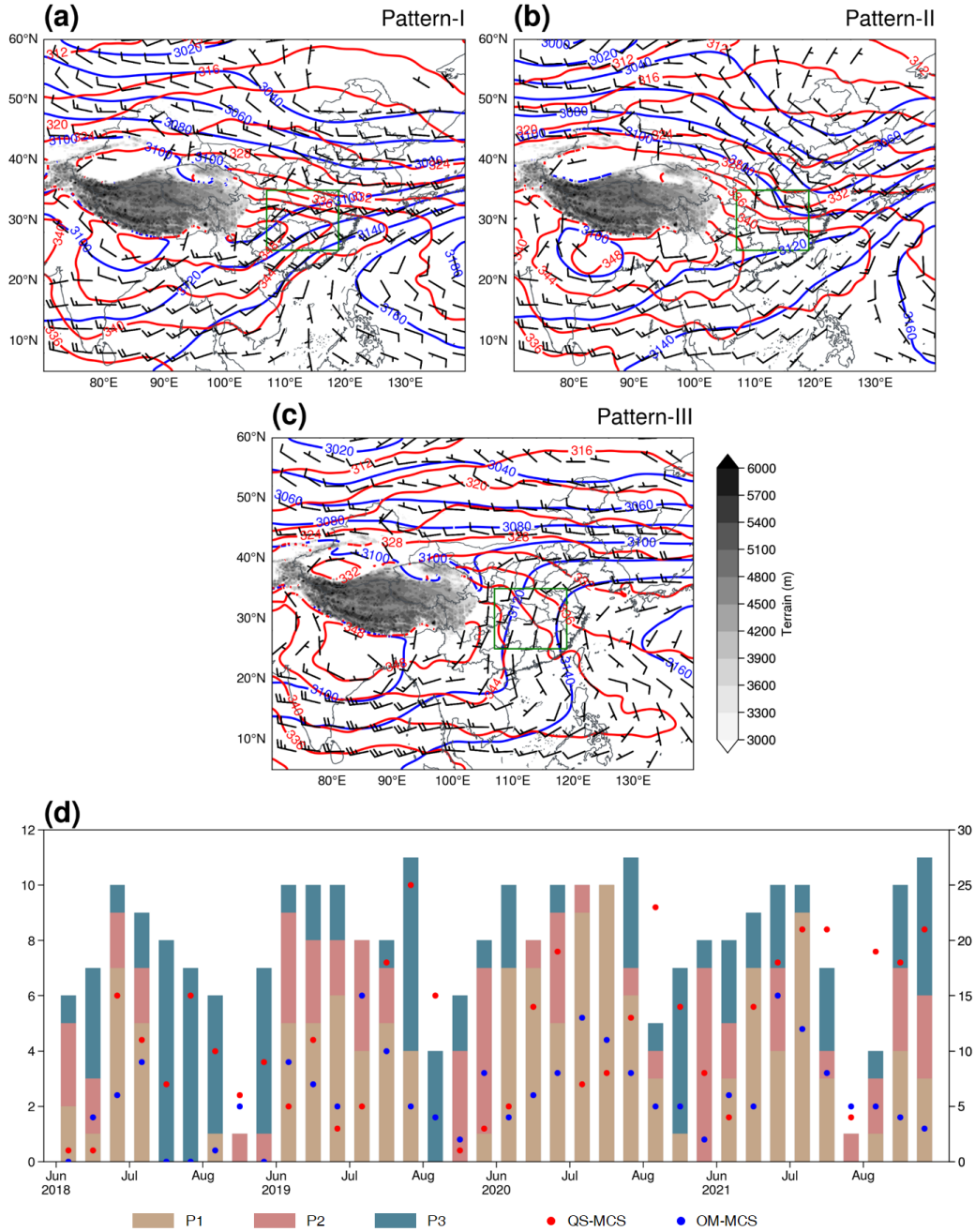
The MCSs in P2 are mostly initiated at the rear of the upper-level troughs, where a synoptic-scale low-level convergence zone/or low-pressure formed by the northerly flow and the southerly flow, favorable for small convective cells merging into a larger MCS (Maurer et al., 2017). As for the role of large-scale circulation in establishing instability, the case-by-case examination shows that in some cases the vertical structures of the upper-level troughs are tilted forward. Under the pattern of P2, the equivalent potential temperature decreases with height, creating convective instability. However, more information along with some in-depth study are required to confirm this conclusion.

A total of 330 QS MCSs and 187 OM MCSs are initiated during JJA of 2018–2021. Fifty percent of QS MCSs and 59.9% of OM MCSs are initiated in P1, suggesting that P1 is favorable for both QS and OM MCS initiation. Thirteen percent (36.1%) of the QS MCSs and 25.7% (14.4%) of the OM MCSs are initiated in P2 (P3). The daily average initiation frequencies of QS MCSs in the three patterns are 1.31, 0.65 and 1.31, and those of the OM MCSs are 0.88, 0.72 and 0.3, respectively. In general, the QS MCS initiation in P1 and P3 is the same and in P2 is the least, while the OM MCSs are initiated the most in P1, followed by P2 and the least in P3.

**Table 1.** The number of days for each pattern and the total and daily occurrence for QS MCSs and OM MCSs in each pattern.

	P1 (128 days)	P2 (66 days)	P3 (91 days)
QS MCS	165 / 1.31	43 / 0.65	119 / 1.31
OM MCS	112 / 0.88	48 / 0.72	27 / 0.3

632       The synoptic-scale circulations in the middle reaches of YRB would be rather  
633 different in association with the several abrupt seasonal transition events during June to  
634 August (Hirasawa et al., 1995; Kawamura & Murakami, 1998; Zhang et al., 2020),  
635 which also affect the characteristics of MCSs' initiation, as being described in  
636 subsection 3.2. To further illustrate the seasonal changes in the appearance frequency  
637 of three circulation patterns and two types of MCSs, a time series in ten-day periods are  
638 shown in Fig. 9d. The occurrence frequency of P1 favors June and July, and that of P2  
639 favors late July and August. As for P3, no notable seasonal changes are found. The  
640 occurrence frequency of OM MCSs peaks in late June or early July, and that of QS  
641 MCSs peaks variously in different years. Note that an extreme Mei-yu season in 2020  
642 (Liu & Ding, 2020), featuring earlier onset, later retreat and abundant accumulated  
643 rainfall, and the occurrence frequencies of both P1 and OM MCSs are high in 2020. For  
644 the abnormal Mei-yu year (with a shorter duration and less rainfall) of 2018 (Zhao,  
645 2019), the occurrence frequencies of both P1 and OM MCSs are lowest, with only one  
646 P1-type circulation and very few OM MCSs occurred after early July in 2018. The  
647 results imply that there are some connections between the Mei-yu front and the  
648 occurrence of P1 and OM MCSs.



649

650 **Figure 9.** The composite geopotential fields (blue contours, gpm), equivalent potential  
 651 temperature fields (red contours, K) and wind fields (wind barbs, m s<sup>-1</sup>) at 700 hPa of  
 652 P1 (a), P2 (b) and P3 (c), respectively. A half (full) barb represents 2 m s<sup>-1</sup> (4 m s<sup>-1</sup>).  
 653 The green rectangle marks the middle reaches of the YRB. The gray shading represents  
 654 terrain heights (m). The bars (scatters) in (d) represent the occurrence frequency of  
 655 three circulation patterns (two types of MCSs) over each ten-day period from June to  
 656 August of 2018–2021, corresponding to the left (right) vertical axis. Note that for July

657 and August, the last ten-day period has 11 days.

#### 658 4.2. Environmental parameters

659 To investigate the dynamic and thermodynamic conditions for MCS initiation  
660 under the three circulation patterns, ten environmental parameters are statistically  
661 analyzed, and the results are shown in Fig. 10.

662 The mean value of SBCAPE in P1 (Fig. 10 a) is  $2363 \text{ J kg}^{-1}$  and that of  
663 MUCAPE is  $2491 \text{ J kg}^{-1}$ , both the lowest in the three patterns. A low CAPE often  
664 implies a high LFC height or a small environmental lapse rate, yet the LFC height in P1  
665 is the lowest in the three patterns (Fig. 10g) with a mean value of 743 m, which suggests  
666 that the lapse rate of the mid-low troposphere in P1 is small. The mean value of LI in P1  
667 (Fig. 10e) is  $-4.4 \text{ K}$ , the highest in the three patterns, which also confirms this  
668 conclusion. The mean PW in P1 (Fig. 10h) is 65 mm, which is significantly higher than  
669 those in P2 and P3. The contribution to the local water vapor growth in the YRB often  
670 came from the southwesterly and southeasterly originating from the oceans (Li et al.,  
671 2014; Shi et al., 2020; Wang et al., 2021), which is consistent with the synoptic  
672 circulation in P1.

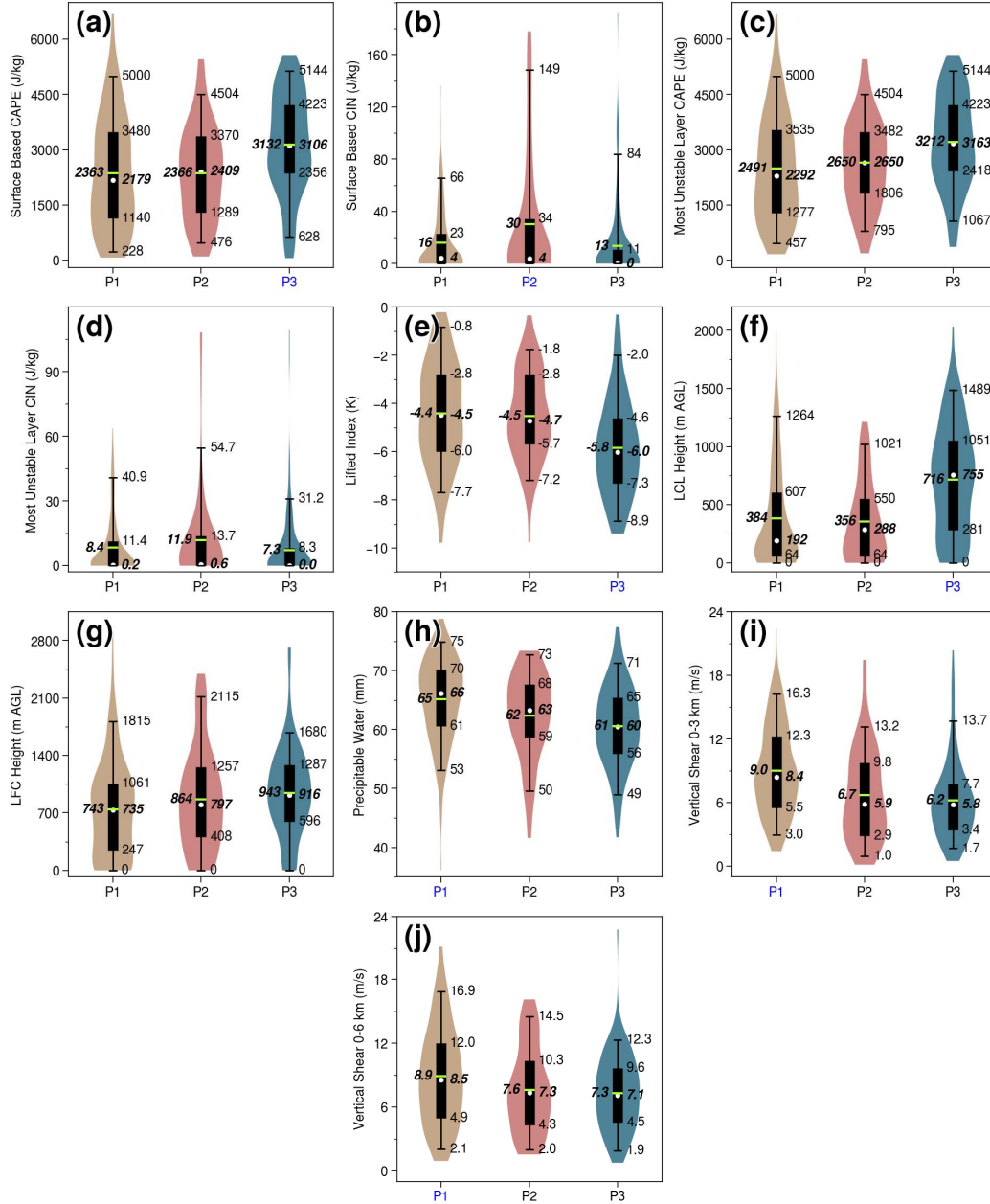
673 The mean SHR3 (Fig. 10i) and SHR6 (Fig. 10j) in P1 are  $9 \text{ m s}^{-1}$  and  $8.9 \text{ m s}^{-1}$ ,  
674 respectively, which are both significantly higher than those in P2 and P3. In P2 and P3,  
675 the SHR6s are basically  $1 \text{ m s}^{-1}$  higher than the SHR3s (both the median and mean  
676 value). However, in P1, the medians of SHR6 and SHR3 are basically equal, and the  
677 mean values of SHR6 are even lower than those of SHR3. There is little difference  
678 between SHR3 and SHR6 in P1, but the SHR6s in P2 and P3 are higher than the  
679 SHR3s, which suggests that the wind speed in the low troposphere in P1 is high or that  
680 MCS initiation in P1 may often be accompanied by low-level jets. Higher vertical wind  
681 shears in P1 may be the reason why OM MCSs tend to occur in P1 (Cohen et al., 2007).

682 The mean SBCAPE (MUCAPE) in P2 is  $2366 \text{ J kg}^{-1}$  ( $2650 \text{ J kg}^{-1}$ ). The  
683 difference between MUCAPE and SBCAPE in P2 is the largest among the three  
684 patterns, indicating that the atmosphere in the boundary layer in P2 is more stable than  
685 those in P1 and P3, which is consistent with the composite circulation in P2, dominated  
686 by northerlies. In operational forecasts, a stable boundary layer and a low CAPE can be  
687 misleading and cause the possible elevated convections to be ignored. The mean

688 SBCIN in P2 is  $30 \text{ J kg}^{-1}$  (Fig. 10b), and the mean MUCIN in P2 is  $11.9 \text{ J kg}^{-1}$  (Fig.  
 689 10d), and both SBCIN and MUCIN were significantly higher than those in P1 and P3.  
 690 In P2, 25% of MCSs are initiated in the environment with SBCIN greater than  $34 \text{ J kg}^{-1}$   
 691 (Fig. 10b). The large SBCIN in P2 confirms the aforementioned conclusion that the  
 692 low-level atmosphere in P2 is more stable than those in P1 and P3. The mean LCL  
 693 height in P2 (Fig. 10f) is 356 m, which is the lowest among the three patterns, and the  
 694 mean LFC height (Fig. 10g) is 864 m. The lowest LCL height in P2 indicates a high  
 695 relative humidity at the surface, which may be caused by the cold invasion related to the  
 696 northerly.

697 Both the mean SBCAPE (Fig. 10a) and the mean MUCAPE (Fig. 10c) in P3 are  
 698  $3132 \text{ J kg}^{-1}$  and are significantly higher than those in P1 and P2. More than 25% of  
 699 MCSs are initiated in the environment with SBCAPE over  $4000 \text{ J kg}^{-1}$ . The mean PW  
 700 in P3 (Fig. 10h) is 61 mm, the mean SHR3 (Fig. 10i) is  $6.2 \text{ m s}^{-1}$ , and the mean SHR6  
 701 (Fig. 10j) is  $7.3 \text{ m s}^{-1}$ . Although different environmental parameters are not simply  
 702 compensated for each other (Kirkpatrick et al., 2007), considering the lack of synoptic  
 703 forcing and the lowest PW (Fig. 10j) in P3, a higher CAPE may be required during  
 704 MCS initiation (Kirkpatrick et al., 2009; McCaul & Weisman, 2001). Furthermore, it is  
 705 suggested that in an environment with a large CAPE, a higher LFC height and a lower  
 706 PW are beneficial for updrafts (Kirkpatrick et al., 2011), which is similar to the  
 707 configuration in P3. The mean LCL height (Fig. 10f) is 716 m and is significantly  
 708 higher than those in P1 and P2. The highest LCL height in P3 suggests a relatively dry  
 709 boundary layer (Rasmussen & Blanchard, 1998), causing stronger evaporation and  
 710 colder outflow from the downdrafts (Kuchera & Parker, 2006) and further resulting in  
 711 severe wind on the surface ground (Evans & Doswell, 2001; Kaltenböck et al., 2009).  
 712 The difference between the mean LFC height and the mean LCL height is smallest in  
 713 P3. A high LCL height suggests a dry low-level environment, and a low LFC height  
 714 represents a large lapse rate, which indicates that in the warm and moist air mass, the  
 715 surface solar heating in the afternoon leads to the high surface temperature and large  
 716 lapse rate in the boundary layer, favoring the initiation of MCSs. The mean SBCIN  
 717 (Fig. 10b) is  $13 \text{ J kg}^{-1}$ , and the mean MUCIN (Fig. 10d) is  $7.3 \text{ J kg}^{-1}$ , and both are at the  
 718 minimum in the 3 patterns. Note that the medians of the SBCIN and the MUCIN in P3  
 719 are both  $0 \text{ J kg}^{-1}$ , which suggests that more than half of the MCSs in P3 are initiated in  
 720 the environment with no CIN. However, the mean LFC height in P3 is the highest,

721 combined with the minimum CIN, representing a dry-adiabatic or even superadiabatic  
722 low-level atmosphere.



723

724 **Figure 10.** Violin plots of environmental parameters. From (a) to (j) are SBCAPE ( $\text{J kg}^{-1}$ )  
725  $\text{kg}^{-1}$ ), SBCIN ( $\text{J kg}^{-1}$ ), MUCAPE ( $\text{J kg}^{-1}$ ), MUCIN ( $\text{J kg}^{-1}$ ), LI (K), LCL (m), LFC (m),  
726 PW (mm), SHR3 ( $\text{m s}^{-1}$ ), and SHR6 ( $\text{m s}^{-1}$ ). The outline of the violin represents the  
727 probability density. The upper and lower edges (caps) of the box (whiskers) inside the  
728 violin represent the 3rd and 1st quartiles (95th and 5th percentiles), respectively, which  
729 are marked on the right side of the violin. The white dot (lemon dash) inside the box



represents the median (mean value), which is marked in bold italics on the right (left). The pattern label marked blue indicates that the mean value of the parameter in this pattern is significantly (above the 95% level based on a two-tailed Welch's *t*-test) different from those in the other two patterns.

## 5 Summary and conclusions

Based on the BT data from the Advanced Geosynchronous Radiation Imager onboard the FY-4A satellite during the warm seasons (April–September) of 2018–2021, the combination of areal overlapping and optical flow is adopted to identify and track the MCSs in the middle reaches of the YRB, which are categorized into the quasistationary (QS) type and the outward-moving (OM) type and are statistically analyzed. The daily circulations of JJA, during which MCSs occur most frequently, are objectively classified into three patterns using the *k-means* algorithm, and the environmental conditions of MCS initiation are further compared and analyzed. The main conclusions are described as follows:

(1) During the warm seasons of 2018–2021, 524 QS MCSs and 276 OM MCSs are identified in the middle reaches of the YRB. Among the four kinds of main moving paths (i.e., northeast kind, southeast kind, northwest kind and southwest kind) of QS MCSs, the occurrence frequency in the southeast kind is the highest. The QS MCSs are mostly initiated over mountainous areas and then propagate to the plains. The moving trajectories of OM MCSs are classified into three kinds of paths, namely, the northeast kind, the southeast kind and the southwest kind, among which the southeast kind has the largest amount of OM MCSs.

(2) The QS MCSs primarily occur in July and August and are mainly initiated in the afternoon (0600–0700 UTC). The OM MCSs mostly occur in June and July with two initiation peaks at noon (0300–0500 UTC) and late night (1800–1900 UTC), respectively, corresponding to the afternoon peak and morning peak of the typical precipitation associated with Mei-yu fronts. QS MCSs are mainly initiated in mountainous areas, while OM MCSs are mostly triggered in plain areas.

(3) The OM MCSs move faster than the QS MCSs and mostly propagate eastward. The durations and maximum extents of QS MCSs show no obvious differences among different months, while those of OM MCSs vary among different

months. The lowest brightness temperatures of QS MCSs mostly appear in the afternoon (0800–0900 UTC), but those of the OM MCSs exhibit no obvious diurnal variation. Compared to the OM MCSs, the QS MCSs show notable diurnal variation in intensity and develop more rapidly.

(4) Circulations at 0000 UTC of 285 MCS days, without direct influences from tropical cyclones, are classified into 3 patterns using the k-means algorithm. The composite circulation of P1 is consistent with the typical circulation of the Mei-yu front, and those of P2 and P3 are dominated by the northwesterly and the weak southerly, respectively. The mean initiation frequencies of the QS MCSs in P1 and P3 are the same and that in P2 is the lowest. The OM MCSs are initiated the most in P1, followed by P2, and they are initiated the least in P3.

(5) Analysis of the environmental conditions favorable for MCS initiation in the three circulation patterns suggests that a) the low-level wind speed in P1 is relatively high, and the MCS initiations in P1 may be accompanied by low-level jets, which is more favorable for OM MCS initiation and propagation; b) the circulation in P2 is dominated by northwesterlies with a relatively stable layer in the low-level troposphere; and c) surface solar heating in P3 establishes a dry-adiabatic or even a superadiabatic layer and further lowers the stability.

In the present work, a comprehensive analysis was conducted on the MCSs in the middle reaches of the YRB during the warm seasons of 2018–2021, focusing mainly on the statistical characteristics, circulation patterns, and environmental conditions favorable for MCS initiation, and some conclusions with scientific significance and utility value were obtained. However, some problems remain unsolved. For example, the late-night triggering peak of OM MCSs is not well understood, and the impacts of orography on MCSs in the middle reaches of the YRB need further exploration. Further work will focus on these issues.

## Acknowledgments

This research was supported by the National Natural Science Foundation of China (Grant U2142202, 41975056 and 41975057).

## Data/Software Availability Statement

Data: The FY-4A BT data is obtained from

<http://satellite.nsmc.org.cn/PortalSite/Data/Satellite.aspx> (Yang et al., 2017) with approval by the China Meteorological Administration. The TC best-track data is available at [https://tcdata.typhoon.org.cn/zjljsjj\\_zlhq.html](https://tcdata.typhoon.org.cn/zjljsjj_zlhq.html) (Lu et al., 2021; Ying et al., 2014). Both of the above sites include translation functionality. The ERA5 hourly data on pressure levels is available at <https://doi.org/10.24381/cds.bd0915c6> (Hersbach et al., 2020). The ERA5 hourly data on single levels is available at <https://doi.org/10.24381/cds.adbb2d47> (Hersbach et al., 2020).

Software: Figures were made with ProPlot version 0.9.5 (Davis, 2021), licensed under CC-BY 4.0, available at <https://zenodo.org/record/5602155>. The optical flow was calculated by using OpenCV version 4.7.0 (Bradski, 2000) under the Apache License 2.0, available at <https://opencv.org>. The objective classification was made with scikit-learn version 1.2.2 (Pedregosa et al., 2011), available at <https://scikit-learn.org/stable/>. Environmental parameters were calculated by using MetPy version 1.5.0 (May et al., 2022) available at <https://doi.org/10.5065/D6WW7G29>.

## References

- Akiyama, T. (1989). Large, Synoptic and Meso Scale Variations of the Baiu Front, during July 1982. *Journal of the Meteorological Society of Japan. Ser. II*, 67(1), 57–81. [https://doi.org/10.2151/jmsj1965.67.1\\_57](https://doi.org/10.2151/jmsj1965.67.1_57)
- Asai, T., Ke, S., & Kodama, Y.-M. (1998). Diurnal Variability of Cloudiness over East Asia and the Western Pacific Ocean as Revealed by GMS during the Warm Season. *Journal of the Meteorological Society of Japan. Ser. II*, 76(5), 675–684. [https://doi.org/10.2151/jmsj1965.76.5\\_675](https://doi.org/10.2151/jmsj1965.76.5_675)
- Astling, E. G. (1984). On the relationship between diurnal mesoscale circulations and precipitation in a mountain valley. *Journal of Applied Meteorology and Climatology*, 23(12), 1635–1644. [https://doi.org/10.1175/1520-0450\(1984\)023<1635:OTRBDM>2.0.CO;2](https://doi.org/10.1175/1520-0450(1984)023<1635:OTRBDM>2.0.CO;2)
- Augustine, J. A., & Howard, K. W. (1988). Mesoscale convective complexes over the United States during 1985. *Monthly Weather Review*, 116(3), 685–701.

- 821 [https://doi.org/10.1175/1520-0493\(1988\)116<0685:MCCOTU>2.0.CO;2](https://doi.org/10.1175/1520-0493(1988)116<0685:MCCOTU>2.0.CO;2)
- 822 Bai, L., Chen, G., & Huang, L. (2020). Convection initiation in monsoon coastal areas  
823 (South China). *Geophysical Research Letters*, 47(11), e2020GL087035.  
824 <https://doi.org/10.1029/2020GL087035>
- 825 Bao, X., Zhang, F., & Sun, J. (2011). Diurnal variations of warm-season precipitation  
826 east of the Tibetan Plateau over China. *Monthly Weather Review*, 139(9), 2790–  
827 2810. <https://doi.org/10.1175/MWR-D-11-00006.1>
- 828 Bechini, R., & Chandrasekar, V. (2017). An enhanced optical flow technique for radar  
829 nowcasting of precipitation and winds. *Journal of Atmospheric and Oceanic*  
830 *Technology*, 34(12), 2637–2658. <https://doi.org/10.1175/JTECH-D-17-0110.1>
- 831 Bernard, E., Naveau, P., Vrac, M., & Mestre, O. (2013). Clustering of maxima: spatial  
832 dependencies among heavy rainfall in France. *Journal of Climate*, 26(20), 7929–  
833 7937. <https://doi.org/10.1175/JCLI-D-12-00836.1>
- 834 Bister, M. (2001). Effect of peripheral convection on tropical cyclone formation.  
835 *Journal of the Atmospheric Sciences*, 58(22), 3463–3476.  
836 [https://doi.org/10.1175/1520-0469\(2001\)058<3463:EOPCOT>2.0.CO;2](https://doi.org/10.1175/1520-0469(2001)058<3463:EOPCOT>2.0.CO;2)
- 837 Bowler, N. E. H., Pierce, C. E., & Seed, A. (2004). Development of a precipitation  
838 nowcasting algorithm based upon optical flow techniques. *Journal of Hydrology*,  
839 288(1–2), 74–91. <https://doi.org/10.1016/j.jhydrol.2003.11.011>
- 840 Bradski, G. (2000). The OpenCV library. *Dr. Dobb's Journal of Software Tools*.  
841 <https://www.drdobbs.com/open-source/the-opencv-library/184404319>
- 842 Brooks, H. E., Lee, J. W., & Craven, J. P. (2003). The spatial distribution of severe  
843 thunderstorm and tornado environments from global reanalysis data. *Atmospheric*  
844 *Research*, 67–68, 73–94. [https://doi.org/10.1016/S0169-8095\(03\)00045-0](https://doi.org/10.1016/S0169-8095(03)00045-0)
- 845 Brotzge, J. A., Nelson, S. E., Thompson, R. L., & Smith, B. T. (2013). Tornado  
846 probability of detection and lead time as a function of convective mode and  
847 environmental parameters. *Weather and Forecasting*, 28(5), 1261–1276.  
848 <https://doi.org/10.1175/WAF-D-12-00119.1>

- 849 Burton, R. R., Blyth, A. M., Cui, Z., Groves, J., Lamprey, B. L., Fletcher, J. K.,  
850 Marsham, J.H., Parker, D.J. & Roberts, A. (2022). Satellite-based nowcasting of  
851 west African mesoscale storms has skill at up to 4-h lead time. *Weather and*  
852 *Forecasting*, 37(4), 445–455. <https://doi.org/10.1175/WAF-D-21-0051.1>
- 853 Carbone, R. E., Tuttle, J. D., Ahijevych, D. A., & Trier, S. B. (2002). Inferences of  
854 predictability associated with warm season precipitation episodes. *Journal of the*  
855 *Atmospheric Sciences*, 59(13), 2033–2056.  
856 [https://doi.org/10.1175/1520-0469\(2002\)059<2033:IOPAWW>2.0.CO;2](https://doi.org/10.1175/1520-0469(2002)059<2033:IOPAWW>2.0.CO;2)
- 857 Cohen, A. E., Coniglio, M. C., Corfidi, S. F., & Corfidi, S. J. (2007). Discrimination of  
858 mesoscale convective system environments using sounding observations. *Weather*  
859 *and Forecasting*, 22(5), 1045–1062. <https://doi.org/10.1175/WAF1040.1>
- 860 Davis, L. L. B. (2021, October). ProPlot (Version 0.9.5). [Software]. *Zenodo*.  
861 <https://doi.org/10.5281/zenodo.5602155>
- 862 Dong, Y., Li, J., Guo, J., Jiang, Z., Chu, Y., Chang, L., Yang, Y. & Liao, H. (2020). The  
863 impact of synoptic patterns on summertime ozone pollution in the North China  
864 Plain. *Science of The Total Environment*, 735, 139559.  
865 <https://doi.org/10.1016/j.scitotenv.2020.139559>
- 866 Evans, J. S., & Doswell, C. A. (2001). Examination of derecho environments using  
867 proximity soundings. *Weather and Forecasting*, 16(3), 329–342.  
868 [https://doi.org/10.1175/1520-0434\(2001\)016<0329:EODEUP>2.0.CO;2](https://doi.org/10.1175/1520-0434(2001)016<0329:EODEUP>2.0.CO;2)
- 869 Feng, Z., Leung, L. R., Houze, R. A., Hagos, S., Hardin, J., Yang, Q., Han, B. & Fan, J.  
870 (2018). Structure and evolution of mesoscale convective systems: sensitivity to  
871 cloud microphysics in convection-permitting simulations over the United States.  
872 *Journal of Advances in Modeling Earth Systems*, 10(7), 1470–1494.  
873 <https://doi.org/10.1029/2018MS001305>
- 874 Feng, Z., Houze, R. A., Leung, L. R., Song, F., Hardin, J. C., Wang, J., Gustafson, W. I.  
875 & Homeyer, C. R. (2019). Spatiotemporal characteristics and large-scale  
876 environments of mesoscale convective systems east of the Rocky Mountains.  
877 *Journal of Climate*, 32(21), 7303–7328. <https://doi.org/10.1175/JCLI-D-19-0137.1>

- 878 Fu, S., Sun, J., Zhao, S., & Li, W. (2011a). The energy budget of a southwest vortex  
879 with heavy rainfall over south China. *Advances in Atmospheric Sciences*, 28(3),  
880 709–724. <https://doi.org/10.1007/s00376-010-0026-z>
- 881 Fu, S., Sun, J., Zhao, S., Li, W. & Li, B. (2011b). A study of the impacts of the eastward  
882 propagation of convective cloud systems over the Tibetan Plateau on the rainfall of  
883 the Yangtze-Huai River basin. *Acta Meteorologica Sinica*, 69(4), 581–600,  
884 <http://doi.org/10.11676/qxxb2011.051>. (in Chinese)
- 885 Gallus, W. A., Snook, N. A., & Johnson, E. V. (2008). Spring and summer severe  
886 weather reports over the Midwest as a function of convective mode: a preliminary  
887 study. *Weather and Forecasting*, 23(1), 101–113.  
888 <https://doi.org/10.1175/2007WAF2006120.1>
- 889 Gensini, V. A., Mote, T. L., & Brooks, H. E. (2014). Severe-thunderstorm reanalysis  
890 environments and collocated radiosonde observations. *Journal of Applied*  
891 *Meteorology and Climatology*, 53(3), 742–751.  
892 <https://doi.org/10.1175/JAMC-D-13-0263.1>
- 893 Grams, J. S., Thompson, R. L., Snively, D. V., Prentice, J. A., Hodges, G. M., &  
894 Reames, L. J. (2012). A climatology and comparison of parameters for significant  
895 tornado events in the United States. *Weather and Forecasting*, 27(1), 106–123.  
896 <https://doi.org/10.1175/WAF-D-11-00008.1>
- 897 He, H., & Zhang, F. (2010). Diurnal variations of warm-season precipitation over  
898 northern China. *Monthly Weather Review*, 138(4), 1017–1025.  
899 <https://doi.org/10.1175/2010MWR3356.1>
- 900 He, Z., Zhang, Q., Bai, L., & Meng, Z. (2017). Characteristics of mesoscale convective  
901 systems in central East China and their reliance on atmospheric circulation patterns.  
902 *International Journal of Climatology*, 37(7), 3276–3290.  
903 <https://doi.org/10.1002/joc.4917>
- 904 Hendricks, E. A., & Montgomery, M. T. (2006). Rapid scan views of convectively  
905 generated mesovortices in sheared tropical cyclone Gustav (2002). *Weather and*  
906 *Forecasting*, 21(6), 1041–1050. <https://doi.org/10.1175/WAF950.1>

- 907 Hersbach, H., Bell, B., Berrisford, P., Hirahara, S., Horányi, A., Muñoz-Sabater, J., et al.  
908 (2020). The ERA5 global reanalysis. *Quarterly Journal of the Royal*  
909 *Meteorological Society*, 146(730), 1999–2049. <https://doi.org/10.1002/qj.3803>
- 910 Hirasawa, N., Kato, K., & Takeda, T. (1995). Abrupt Change in the Characteristics of  
911 the Cloud Zone in Subtropical East Asia around the Middle of May. *Journal of the*  
912 *Meteorological Society of Japan. Ser. II*, 73(2), 221–239.  
913 [https://doi.org/10.2151/jmsj1965.73.2\\_221](https://doi.org/10.2151/jmsj1965.73.2_221)
- 914 Hoffmann, P., & Schlünzen, K. H. (2013). Weather pattern classification to represent  
915 the urban heat island in present and future climate. *Journal of Applied Meteorology*  
916 *and Climatology*, 52(12), 2699–2714. <https://doi.org/10.1175/JAMC-D-12-065.1>
- 917 Houze, R. A. (2004). Mesoscale convective systems. *Reviews of Geophysics*, 42(4).  
918 <https://doi.org/10.1029/2004RG000150>
- 919 Huth, R., Beck, C., Philipp, A., Demuzere, M., Ustrnul, Z., Cahynová, M., et al. (2008).  
920 Classifications of atmospheric circulation patterns. *Annals of the New York*  
921 *Academy of Sciences*, 1146(1), 105–152. <https://doi.org/10.1196/annals.1446.019>
- 922 Jiang, J. & Fan, M. (2002). Convective clouds and mesoscale convective systems over  
923 the Tibetan Plateau in summer. *Chinese Journal of Atmospheric Sciences*, 26(2),  
924 263–270, <http://doi.org/10.3878/j.issn.1006-9895.2002.02.12>. (in Chinese)
- 925 Kaltenböck, R., Diendorfer, G., & Dotzek, N. (2009). Evaluation of thunderstorm  
926 indices from ECMWF analyses, lightning data and severe storm reports.  
927 *Atmospheric Research*, 93(1), 381–396. [https://doi.org/10.1016/](https://doi.org/10.1016/j.atmosres.2008.11.005)  
928 [j.atmosres.2008.11.005](https://doi.org/10.1016/j.atmosres.2008.11.005)
- 929 Kanungo, T., Mount, D. M., Netanyahu, N. S., Piatko, C. D., Silverman, R., & Wu, A. Y.  
930 (2002). An efficient k-means clustering algorithm: analysis and implementation.  
931 *IEEE Transactions on Pattern Analysis and Machine Intelligence*, 24(7), 881–892.  
932 <https://doi.org/10.1109/TPAMI.2002.1017616>
- 933 Kato, K., Matsumoto, J., & Iwasaki, H. (1995). Diurnal Variation of Cb-Clusters over  
934 China and Its Relation to Large-Scale Conditions in the Summer of 1979. *Journal*  
935 *of the Meteorological Society of Japan. Ser. II*, 73(6), 1219–1234.

- 936 [https://doi.org/10.2151/jmsj1965.73.6\\_1219](https://doi.org/10.2151/jmsj1965.73.6_1219)
- 937 Kawamura, R., & Murakami, T. (1998). Baiu near Japan and Its Relation to Summer  
938 Monsoons over Southeast Asia and the Western North Pacific. *Journal of the*  
939 *Meteorological Society of Japan. Ser. II*, 76(4), 619–639.  
940 [https://doi.org/10.2151/jmsj1965.76.4\\_619](https://doi.org/10.2151/jmsj1965.76.4_619)
- 941 King, A. T., & Kennedy, A. D. (2019). North American supercell environments in  
942 atmospheric reanalyses and RUC-2. *Journal of Applied Meteorology and*  
943 *Climatology*, 58(1), 71–92. <https://doi.org/10.1175/JAMC-D-18-0015.1>
- 944 Kirkpatrick, J. C., McCaul, E. W., & Cohen, C. (2007). The motion of simulated  
945 convective storms as a function of basic environmental parameters. *Monthly*  
946 *Weather Review*, 135(9), 3033–3051. <https://doi.org/10.1175/MWR3447.1>
- 947 Kirkpatrick, J. C., McCaul, E. W., & Cohen, C. (2009). Variability of updraft and  
948 downdraft characteristics in a large parameter space study of convective storms.  
949 *Monthly Weather Review*, 137(5), 1550–1561. [https://doi.org/10.1175/](https://doi.org/10.1175/2008MWR2703.1)  
950 [2008MWR2703.1](https://doi.org/10.1175/2008MWR2703.1)
- 951 Kirkpatrick, J. C., McCaul, E. W., & Cohen, C. (2011). Sensitivities of simulated  
952 convective storms to environmental CAPE. *Monthly Weather Review*, 139(11),  
953 3514–3532. <https://doi.org/10.1175/2011MWR3631.1>
- 954 Kolios, S., & Feidas, H. (2010). A warm season climatology of mesoscale convective  
955 systems in the Mediterranean basin using satellite data. *Theoretical and Applied*  
956 *Climatology*, 102(1–2), 29–42. <https://doi.org/10.1007/s00704-009-0241-7>
- 957 Ku, H.-Y., Noh, N., Jeong, J.-H., Koo, J.-H., Choi, W., Kim, B.-M., et al. (2021).  
958 Classification of large-scale circulation patterns and their spatio-temporal  
959 variability during High-PM10 events over the Korean Peninsula. *Atmospheric*  
960 *Environment*, 262, 118632. <https://doi.org/10.1016/j.atmosenv.2021.118632>
- 961 Kubota, H., & Nitta, T. (2001). Diurnal variations of tropical convection observed  
962 during the TOGA-COARE. *Journal of the Meteorological Society of Japan. Ser. II*,  
963 79(3), 815–830. <https://doi.org/10.2151/jmsj.79.815>



- 964 Kuchera, E. L., & Parker, M. D. (2006). Severe convective wind environments.  
965 *Weather and Forecasting*, 21(4), 595–612. <https://doi.org/10.1175/WAF931.1>
- 966 Kukulies, J., Chen, D., & Curio, J. (2021). The role of mesoscale convective systems in  
967 precipitation in the Tibetan Plateau region. *Journal of Geophysical Research:*  
968 *Atmospheres*, 126(23), e2021JD035279. <https://doi.org/10.1029/2021JD035279>
- 969 Laing, A. G., & Michael Fritsch, J. (1997). The global population of mesoscale  
970 convective complexes. *Quarterly Journal of the Royal Meteorological Society*,  
971 123(538), 389–405. <https://doi.org/10.1002/qj.49712353807>
- 972 Lewis, M. W., & Gray, S. L. (2010). Categorisation of synoptic environments  
973 associated with mesoscale convective systems over the UK. *Atmospheric Research*,  
974 97(1–2), 194–213. <https://doi.org/10.1016/j.atmosres.2010.04.001>
- 975 Li, J., Yu, R., Zhou, T., & Wang, B. (2005). Why is there an early spring cooling shift  
976 downstream of the Tibetan Plateau? *Journal of Climate*, 18(22), 4660–4668.  
977 <https://doi.org/10.1175/JCLI3568.1>
- 978 Li, X., Zhou, W., Chen, D., Li, C., & Song, J. (2014). Water vapor transport and  
979 moisture budget over eastern China: remote forcing from the two types of El Niño.  
980 *Journal of Climate*, 27(23), 8778–8792.  
981 <https://doi.org/10.1175/JCLI-D-14-00049.1>
- 982 Li, Y., Wang, Y., Yang, S., Hu, L., Gao, S., & Fu, R. (2008). Characteristics of summer  
983 convective systems initiated over the Tibetan Plateau. Part I: origin, track,  
984 development, and precipitation. *Journal of Applied Meteorology and Climatology*,  
985 47(10), 2679–2695. <https://doi.org/10.1175/2008JAMC1695.1>
- 986 Li, Z., Takeda, T., Tsuboki, K., Kato, K., Kawashima, M., & Fujiyoshi, Y. (2007).  
987 Nocturnal evolution of cloud clusters over eastern China during the intensive  
988 observation periods of GAME/HUBEX in 1998 and 1999. *Journal of the*  
989 *Meteorological Society of Japan. Ser. II*, 85(1), 25–45.  
990 <https://doi.org/10.2151/jmsj.85.25>
- 991 Lin, X., Randall, D. A., & Fowler, L. D. (2000). Diurnal variability of the hydrologic  
992 cycle and radiative fluxes: comparisons between observations and a GCM. *Journal*

- 993 of *Climate*, 13(23), 4159–4179. [https://doi.org/10.1175/1520-0442\(2000\)](https://doi.org/10.1175/1520-0442(2000)013<4159:DVOTHC>2.0.CO;2)  
994 [013<4159:DVOTHC>2.0.CO;2](https://doi.org/10.1175/1520-0442(2000)013<4159:DVOTHC>2.0.CO;2)
- 995 Liu, N., Zhou, S., Liu, C., & Guo, J. (2019). Synoptic circulation pattern and boundary  
996 layer structure associated with PM2.5 during wintertime haze pollution episodes in  
997 Shanghai. *Atmospheric Research*, 228, 186–195.  
998 <https://doi.org/10.1016/j.atmosres.2019.06.001>
- 999 Liu, Y., & Ding, Y. (2020). Characteristics and possible causes for the extreme Meiyu  
1000 in 2020. *Meteorological Monthly*, 46(11), 1393–1404.  
1001 <https://doi.org/10.7519/j.issn.1000-0526.2020.11.001> (in Chinese).
- 1002 Lu, X., Yu, H., Ying, M., Zhao, B., Zhang, S., Lin, L., et al. (2021). Western North  
1003 Pacific tropical cyclone database created by the China Meteorological  
1004 Administration. *Advances in Atmospheric Sciences*, 38(4), 690–699.  
1005 <https://doi.org/10.1007/s00376-020-0211-7>
- 1006 Luo, Y., & Chen, Y. (2015). Investigation of the predictability and physical mechanisms  
1007 of an extreme-rainfall-producing mesoscale convective system along the Meiyu  
1008 front in East China: An ensemble approach. *Journal of Geophysical Research:*  
1009 *Atmospheres*, 120(20), 10,593–10,618. <https://doi.org/10.1002/2015JD023584>
- 1010 Luo, Y., Wu, M., Ren, F., Li, J., & Wong, W.-K. (2016). Synoptic situations of extreme  
1011 hourly precipitation over China. *Journal of Climate*, 29(24), 8703–8719.  
1012 <https://doi.org/10.1175/JCLI-D-16-0057.1>
- 1013 Ma, R., Sun, J., & Yang, X. (2021a). A 7-yr climatology of the initiation, decay, and  
1014 morphology of severe convective storms during the warm season over North China.  
1015 *Monthly Weather Review*, 149(8), 2599–2612.  
1016 <https://doi.org/10.1175/MWR-D-20-0087.1>
- 1017 Ma, R., Sun, J., & Yang, X. (2021b). An eight-year climatology of the warm-season  
1018 severe thunderstorm environments over North China. *Atmospheric Research*, 254,  
1019 105519. <https://doi.org/10.1016/j.atmosres.2021.105519>
- 1020 Machado, L. A. T., Rossow, W. B., Guedes, R. L., & Walker, A. W. (1998). Life cycle

- 1021 variations of mesoscale convective systems over the Americas. *Monthly Weather*  
1022 *Review*, 126(6), 1630–1654. [https://doi.org/10.1175/1520-0493\(1998\)126<1630:](https://doi.org/10.1175/1520-0493(1998)126<1630:LCVOMC>2.0.CO;2)  
1023 [LCVOMC>2.0.CO;2](https://doi.org/10.1175/1520-0493(1998)126<1630:LCVOMC>2.0.CO;2)
- 1024 Maddox, R. A. (1980). Mesoscale convective complexes. *Bulletin of the American*  
1025 *Meteorological Society*, 61(11), 1374–1400.  
1026 [https://doi.org/10.1175/1520-0477\(1980\)061<1374:MCC>2.0.CO;2](https://doi.org/10.1175/1520-0477(1980)061<1374:MCC>2.0.CO;2)
- 1027 Mai Z., Fu, S., & Sun, J. (2020). Statistical features of two types of mesoscale  
1028 convective systems (MCSs) generated over the eastern Tibetan Plateau during 16  
1029 consecutive warm seasons. *Climatic and Environmental Research*, 25(4), 385–398,  
1030 <http://doi.org/10.3878/j.issn.1006-9585.2019.19040>. (in Chinese)
- 1031 Marzban, C., & Sandgathe, S. (2010). Optical flow for verification. *Weather and*  
1032 *Forecasting*, 25(5), 1479–1494. <https://doi.org/10.1175/2010WAF2222351.1>
- 1033 Maurer, V., Bischoff-Gauß, I., Kalthoff, N., Gantner, L., Roca, R., & Panitz, H.-J.  
1034 (2017). Initiation of deep convection in the Sahel in a convection-permitting  
1035 climate simulation for northern Africa: Deep Convection in the Sahel. *Quarterly*  
1036 *Journal of the Royal Meteorological Society*, 143(703), 806–816.  
1037 <https://doi.org/10.1002/qj.2966>
- 1038 May, R. M., Goebbert, K. H., Thielen, J. E., Leeman, J. R., Camron, M. D., Bruick, Z.,  
1039 et al. (2022). MetPy: A meteorological python library for data analysis and  
1040 visualization. *Bulletin of the American Meteorological Society*, 103(10), E2273–  
1041 E2284. <https://doi.org/10.1175/BAMS-D-21-0125.1>
- 1042 McCaul, E. W., & Weisman, M. L. (2001). The sensitivity of simulated supercell  
1043 structure and intensity to variations in the shapes of environmental buoyancy and  
1044 shear profiles. *Monthly Weather Review*, 129(4), 664–687. [https://doi.org/10.1175/](https://doi.org/10.1175/1520-0493(2001)129<0664:TSOSSS>2.0.CO;2)  
1045 [1520-0493\(2001\)129<0664:TSOSSS>2.0.CO;2](https://doi.org/10.1175/1520-0493(2001)129<0664:TSOSSS>2.0.CO;2)
- 1046 Mecikalski, J. R., & Bedka, K. M. (2006). Forecasting convective initiation by  
1047 monitoring the evolution of moving cumulus in daytime GOES imagery. *Monthly*  
1048 *Weather Review*, 134(1), 49–78. <https://doi.org/10.1175/MWR3062.1>
- 1049 Meng, Y., Sun, J., Zhang, Y., & Fu, S. (2021). A 10-year climatology of mesoscale

- 1050 convective systems and their synoptic circulations in the southwest mountain area  
1051 of China. *Journal of Hydrometeorology*, 22(1), 23–41. [https://doi.org/10.1175/](https://doi.org/10.1175/JHM-D-20-0167.1)  
1052 [JHM-D-20-0167.1](https://doi.org/10.1175/JHM-D-20-0167.1)
- 1053 Miao, Y., Guo, J., Liu, S., Liu, H., Li, Z., Zhang, W., & Zhai, P. (2017). Classification of  
1054 summertime synoptic patterns in Beijing and their associations with boundary layer  
1055 structure affecting aerosol pollution. *Atmospheric Chemistry and Physics*, 17(4),  
1056 3097–3110. <https://doi.org/10.5194/acp-17-3097-2017>
- 1057 Miller, D., & Fritsch, J. M. (1991). Mesoscale convective complexes in the western  
1058 Pacific region. *Monthly Weather Review*, 119(12), 2978–2992.  
1059 [https://doi.org/10.1175/1520-0493\(1991\)119<2978:MCCITW>2.0.CO;2](https://doi.org/10.1175/1520-0493(1991)119<2978:MCCITW>2.0.CO;2)
- 1060 Morake, D. M., Blamey, R. C., & Reason, C. J. C. (2021). Long-lived mesoscale  
1061 convective systems over eastern South Africa. *Journal of Climate*, 1(aop), 1–66.  
1062 <https://doi.org/10.1175/JCLI-D-20-0851.1>
- 1063 Morel, C., & Senesi, S. (2002). A climatology of mesoscale convective systems over  
1064 Europe using satellite infrared imagery. I: Methodology. *Quarterly Journal of the*  
1065 *Royal Meteorological Society*, 128(584), 1953–1971.  
1066 <https://doi.org/10.1256/003590002320603485>
- 1067 Nga, P. T. T., Ha, P. T., & Hang, V. T. (2021). Satellite-based regionalization of solar  
1068 irradiation in Vietnam by k-Means clustering. *Journal of Applied Meteorology and*  
1069 *Climatology*, 60(3), 391–402. <https://doi.org/10.1175/JAMC-D-20-0070.1>
- 1070 Ning, G., Yim, S. H. L., Yang, Y., Gu, Y., & Dong, G. (2020). Modulations of synoptic  
1071 and climatic changes on ozone pollution and its health risks in mountain-basin areas.  
1072 *Atmospheric Environment*, 240, 117808. [https://doi.org/10.1016/](https://doi.org/10.1016/j.atmosenv.2020.117808)  
1073 [j.atmosenv.2020.117808](https://doi.org/10.1016/j.atmosenv.2020.117808)
- 1074 Panosetti, D., Böing, S., Schlemmer, L., & Schmidli, J. (2016). Idealized large-eddy  
1075 and convection-resolving simulations of moist convection over mountainous terrain.  
1076 *Journal of the Atmospheric Sciences*, 73(10), 4021–4041.  
1077 <https://doi.org/10.1175/JAS-D-15-0341.1>
- 1078 Pedregosa, F., Varoquaux, G., Gramfort, A., Michel, V., Thirion, B., Grisel, O., et al.

- 1079 (2011). Scikit-learn: Machine learning in python. *Journal of Machine Learning*  
1080 *Research*, 12, 2825–2830. <https://dl.acm.org/doi/10.5555/1953048.2078195>
- 1081 Peters, J. M., & Schumacher, R. S. (2014). Objective categorization of  
1082 heavy-rain-producing MCS synoptic types by rotated principal component analysis.  
1083 *Monthly Weather Review*, 142(5), 1716–1737.  
1084 <https://doi.org/10.1175/MWR-D-13-00295.1>
- 1085 Punkka, A.-J., & Bister, M. (2015). Mesoscale convective systems and their  
1086 synoptic-scale environment in Finland. *Weather and Forecasting*, 30(1), 182–196.  
1087 <https://doi.org/10.1175/WAF-D-13-00146.1>
- 1088 Rasmussen, E. N., & Blanchard, D. O. (1998). A baseline climatology of  
1089 sounding-derived supercell and tornado forecast parameters. *Weather and*  
1090 *Forecasting*, 13(4), 1148–1164.  
1091 [https://doi.org/10.1175/1520-0434\(1998\)013<1148:ABCOSD>2.0.CO;2](https://doi.org/10.1175/1520-0434(1998)013<1148:ABCOSD>2.0.CO;2)
- 1092 Rehbein, A., Ambrizzi, T., & Mechoso, C. R. (2018). Mesoscale convective systems  
1093 over the Amazon basin. Part I: climatological aspects. *International Journal of*  
1094 *Climatology*, 38(1), 215–229. <https://doi.org/10.1002/joc.5171>
- 1095 Reif, D. W., & Bluestein, H. B. (2017). A 20-year climatology of nocturnal convection  
1096 initiation over the central and southern Great Plains during the warm season.  
1097 *Monthly Weather Review*, 145(5), 1615–1639.  
1098 <https://doi.org/10.1175/MWR-D-16-0340.1>
- 1099 Roberts, R. D., & Rutledge, S. (2003). Nowcasting storm initiation and growth using  
1100 GOES-8 and WSR-88D data. *Weather and Forecasting*, 18(4), 562–584.  
1101 [https://doi.org/10.1175/1520-0434\(2003\)018<0562:NSIAGU>2.0.CO;2](https://doi.org/10.1175/1520-0434(2003)018<0562:NSIAGU>2.0.CO;2)
- 1102 Rodgers, D. M., Howard, K. W., & Johnston, E. C. (1983). Mesoscale convective  
1103 complexes over the United States during 1982. *Monthly Weather Review*, 111(12),  
1104 2363–2369. [https://doi.org/10.1175/1520-0493\(1983\)111<2363:](https://doi.org/10.1175/1520-0493(1983)111<2363:MCCOTU>2.0.CO;2)  
1105 [MCCOTU>2.0.CO;2](https://doi.org/10.1175/1520-0493(1983)111<2363:MCCOTU>2.0.CO;2)
- 1106 Rodgers, E. B., Chang, S. W., Stout, J., Steranka, J., & Shi, J.-J. (1991). Satellite  
1107 observations of variations in tropical cyclone convection caused by

- 1108 upper-tropospheric troughs. *Journal of Applied Meteorology and Climatology*,  
 1109 30(8), 1163–1184. [https://doi.org/10.1175/1520-0450\(1991\)030<1163:SOOVIT>](https://doi.org/10.1175/1520-0450(1991)030<1163:SOOVIT>2.0.CO;2)  
 1110 [2.0.CO;2](https://doi.org/10.1175/1520-0450(1991)030<1163:SOOVIT>2.0.CO;2)
- 1111 Rousseeuw, P. J. (1987). Silhouettes: A graphical aid to the interpretation and validation  
 1112 of cluster analysis. *Journal of Computational and Applied Mathematics*, 20, 53–65.  
 1113 [https://doi.org/10.1016/0377-0427\(87\)90125-7](https://doi.org/10.1016/0377-0427(87)90125-7)
- 1114 Shen, Y., Du, Y., & Chen, G. (2020). Ensemble sensitivity analysis of heavy rainfall  
 1115 associated with three MCSs coexisting over southern China. *Journal of*  
 1116 *Geophysical Research: Atmospheres*, 125(2). [https://doi.org/10.1029/](https://doi.org/10.1029/2019JD031266)  
 1117 [2019JD031266](https://doi.org/10.1029/2019JD031266)
- 1118 Shi, Y., Jiang, Z., Liu, Z., & Li, L. (2020). A Lagrangian analysis of water vapor sources  
 1119 and pathways for precipitation in East China in different stages of the east Asian  
 1120 summer monsoon. *Journal of Climate*, 33(3), 977–992. [https://doi.org/10.1175/](https://doi.org/10.1175/JCLI-D-19-0089.1)  
 1121 [JCLI-D-19-0089.1](https://doi.org/10.1175/JCLI-D-19-0089.1)
- 1122 Sieglaff, J. M., Cronce, L. M., Feltz, W. F., Bedka, K. M., Pavolonis, M. J., & Heidinger,  
 1123 A. K. (2011). Nowcasting convective storm initiation using satellite-based  
 1124 box-averaged cloud-top cooling and cloud-type trends. *Journal of Applied*  
 1125 *Meteorology and Climatology*, 50(1), 110–126.  
 1126 <https://doi.org/10.1175/2010JAMC2496.1>
- 1127 Solman, S. A., & Menéndez, C. G. (2003). Weather regimes in the South American  
 1128 sector and neighbouring oceans during winter. *Climate Dynamics*, 21(1), 91–104.  
 1129 <https://doi.org/10.1007/s00382-003-0320-x>
- 1130 Song, F., Feng, Z., Leung, L. R., Jr, R. A. H., Wang, J., Hardin, J., & Homeyer, C. R.  
 1131 (2019). Contrasting spring and summer large-scale environments associated with  
 1132 mesoscale convective systems over the U.S. Great Plains. *Journal of Climate*,  
 1133 32(20), 6749–6767. <https://doi.org/10.1175/JCLI-D-18-0839.1>
- 1134 Stahl, K., Moore, R. D., & Mckendry, I. G. (2006). The role of synoptic-scale  
 1135 circulation in the linkage between large-scale ocean–atmosphere indices and winter  
 1136 surface climate in British Columbia, Canada. *International Journal of Climatology*,

- 1137 26(4), 541–560. <https://doi.org/10.1002/joc.1268>
- 1138 Sugimoto, S., & Ueno, K. (2010). Formation of mesoscale convective systems over the  
1139 eastern Tibetan Plateau affected by plateau-scale heating contrasts. *Journal of*  
1140 *Geophysical Research: Atmospheres*, 115. <https://doi.org/10.1029/2009JD013609>
- 1141 Sun, J., & Zhang, F. (2012). Impacts of mountain–plains solenoid on diurnal variations  
1142 of rainfalls along the mei-yu front over the East China plains. *Monthly Weather*  
1143 *Review*, 140(2), 379–397. <https://doi.org/10.1175/MWR-D-11-00041.1>
- 1144 Sun J., Wei J., Fu S., Zhang Y. & Wang H., 2018: The multi-scale physical model for  
1145 persistent heavy rainfall events in the Yangtze-Huaihe River valley. *Chinese*  
1146 *Journal of Atmospheric Sciences*, 42(4), 741–754,  
1147 <http://doi.org/10.3878/j.issn.1006-9895.1803.17246>. (in Chinese)
- 1148 Takeda, T., & Iwasaki, H. (1987). Some Characteristics of Meso-scale Cloud Clusters  
1149 Observed in East Asia between March and October 1980. *Journal of the*  
1150 *Meteorological Society of Japan. Ser. II*, 65(3), 507–513.  
1151 [https://doi.org/10.2151/jmsj1965.65.3\\_507](https://doi.org/10.2151/jmsj1965.65.3_507)
- 1152 Tao, S. (1980). *Heavy Rainfalls in China*. Beijing: Science Press.
- 1153 Ternynck, C., Alaya, M. A. B., Chebana, F., Dabo-Niang, S., & Ouarda, T. B. M. J.  
1154 (2016). Streamflow hydrograph classification using functional data analysis.  
1155 *Journal of Hydrometeorology*, 17(1), 327–344.  
1156 <https://doi.org/10.1175/JHM-D-14-0200.1>
- 1157 Vandal, T., & Nemani, R. (2020). Temporal interpolation of geostationary satellite  
1158 imagery with task specific optical flow. *Proceedings of 1st ACM SIGKDD*  
1159 *Workshop on Deep Learning for Spatiotemporal Data, Applications, and Systems*  
1160 *(DeepSpatial '20)*, 9 pp. [http://mason.gmu.edu/~lzhao9/venues/DeepSpatial2020/](http://mason.gmu.edu/~lzhao9/venues/DeepSpatial2020/papers/DeepSpatial_paper_6_camera_ready.pdf)  
1161 [papers/DeepSpatial\\_paper\\_6\\_camera\\_ready.pdf](http://mason.gmu.edu/~lzhao9/venues/DeepSpatial2020/papers/DeepSpatial_paper_6_camera_ready.pdf)
- 1162 Velasco, I., & Fritsch, J. M. (1987). Mesoscale convective complexes in the Americas.  
1163 *Journal of Geophysical Research: Atmospheres*, 92(D8), 9591–9613.  
1164 <https://doi.org/10.1029/JD092iD08p09591>



- 1165 Wang, H., Sun, J., Fu, S., & Zhang, Y. (2021). Typical circulation patterns and  
1166 associated mechanisms for persistent heavy rainfall events over Yangtze-Huaihe  
1167 River Valley during 1981–2020. *Advances in Atmospheric Sciences*, 38(12), 2167–  
1168 2182. <https://doi.org/10.1007/s00376-021-1194-8>
- 1169 Williams, M., & Houze, R. A. (1987). Satellite-observed characteristics of winter  
1170 monsoon cloud clusters. *Monthly Weather Review*, 115(2), 505–519.  
1171 [https://doi.org/10.1175/1520-0493\(1987\)115<0505:SOCOWM>2.0.CO;2](https://doi.org/10.1175/1520-0493(1987)115<0505:SOCOWM>2.0.CO;2)
- 1172 Wilson, J. W., & Roberts, R. D. (2006). Summary of convective storm initiation and  
1173 evolution during IHOP: observational and modeling perspective. *Monthly Weather*  
1174 *Review*, 134(1), 23–47. <https://doi.org/10.1175/MWR3069.1>
- 1175 Yang, J., Zhang, Z., Wei, C., Lu, F., & Guo, Q. (2017). Introducing the new generation  
1176 of Chinese geostationary weather satellites, Fengyun-4. *Bulletin of the American*  
1177 *Meteorological Society*, 98(8), 1637–1658.  
1178 <https://doi.org/10.1175/BAMS-D-16-0065.1>
- 1179 Yang, J., Zhao, K., Chen, X., Huang, A., Zheng, Y., & Sun, K. (2020). Subseasonal and  
1180 diurnal variability in lightning and storm activity over the Yangtze River Delta,  
1181 China, during mei-yu season. *Journal of Climate*, 33(12), 5013–5033.  
1182 <https://doi.org/10.1175/JCLI-D-19-0453.1>
- 1183 Yang, R., Zhang, Y., Sun, J., & Li, J. (2020). The comparison of statistical features and  
1184 synoptic circulations between the eastward-propagating and quasi-stationary MCSs  
1185 during the warm season around the second-step terrain along the middle reaches of  
1186 the Yangtze River. *Science China Earth Sciences*, 63(8), 1209–1222.  
1187 <https://doi.org/10.1007/s11430-018-9385-3>
- 1188 Yang, X., Fei, J., Huang, X., Cheng, X., Carvalho, L. M. V., & He, H. (2015).  
1189 Characteristics of mesoscale convective systems over China and its vicinity using  
1190 geostationary satellite FY2. *Journal of Climate*, 28(12), 4890–4907.  
1191 <https://doi.org/10.1175/JCLI-D-14-00491.1>
- 1192 Yang, X., & Sun, J. (2018). Organizational modes of severe wind-producing convective  
1193 systems over North China. *Advances in Atmospheric Sciences*, 35(5), 540–549.



- 1194 <https://doi.org/10.1007/s00376-017-7114-2>
- 1195 Yang, Y., Wang, R., Chen, F., Liu, C., Bi, X., & Huang, M. (2021). Synoptic weather  
1196 patterns modulate the frequency, type and vertical structure of summer precipitation  
1197 over Eastern China: a perspective from GPM observations. *Atmospheric Research*,  
1198 249, 105342. <https://doi.org/10.1016/j.atmosres.2020.105342>
- 1199 Ying, M., Zhang, W., Yu, H., Lu, X., Feng, J., Fan, Y., et al. (2014). An overview of the  
1200 China Meteorological Administration tropical cyclone database. *Journal of*  
1201 *Atmospheric and Oceanic Technology*, 31(2), 287–301.  
1202 <https://doi.org/10.1175/JTECH-D-12-00119.1>
- 1203 Yu, R., Zhou, T., Xiong, A., Zhu, Y., & Li, J. (2007). Diurnal variations of summer  
1204 precipitation over contiguous China. *Geophysical Research Letters*, 34(1).  
1205 <https://doi.org/10.1029/2006GL028129>
- 1206 Zhang, A., Chen, Y., Zhou, S., Cui, C., Wan, R., & Fu, Y. (2020). Diurnal variation of  
1207 meiyu rainfall in the Yangtze Plain during atypical meiyu years. *Journal of*  
1208 *Geophysical Research: Atmospheres*, 125(1), e2019JD031742.  
1209 <https://doi.org/10.1029/2019JD031742>
- 1210 Zhang, X., Shen, W., Zhuge, X., Yang, S., Chen, Y., Wang, Y., Chen, T., & Zhang, S.  
1211 (2021). Statistical characteristics of mesoscale convective systems initiated over the  
1212 Tibetan Plateau in summer by Fengyun satellite and precipitation estimates. *Remote*  
1213 *Sensing*, 13(9). <https://doi.org/10.3390/rs13091652>
- 1214 Zhang, X., Wang, X. L., & Corte-Real, J. (1997). On the relationships between daily  
1215 circulation patterns and precipitation in Portugal. *Journal of Geophysical Research:*  
1216 *Atmospheres*, 102(D12), 13495–13507. <https://doi.org/10.1029/97JD01012>
- 1217 Zhang, Y., & Sun, J. (2017). Comparison of the diurnal variations of precipitation east  
1218 of the Tibetan Plateau among sub-periods of Meiyu season. *Meteorology and*  
1219 *Atmospheric Physics*, 129(5), 539–554.  
1220 <https://doi.org/10.1007/s00703-016-0484-7>
- 1221 Zhang, Y., Zhang, F., & Sun, J. (2014). Comparison of the diurnal variations of  
1222 warm-season precipitation for East Asia vs. North America downstream of the

- 1223 Tibetan Plateau vs. the Rocky Mountains. *Atmospheric Chemistry and Physics*,  
1224 14(19), 10741–10759. <https://doi.org/10.5194/acp-14-10741-2014>
- 1225 Zhang, Y., Zhang, F., Davis, C. A., & Sun, J. (2018). Diurnal evolution and structure of  
1226 long-lived mesoscale convective vortices along the mei-yu front over the East  
1227 China plains. *Journal of the Atmospheric Sciences*, 75(3), 1005–1025.  
1228 <https://doi.org/10.1175/JAS-D-17-0197.1>
- 1229 Zhao, X. (2019). Characteristics and Causes Analysis of Abnormal Meiyu in China in  
1230 2018. *Meteorological and Environmental Sciences*, 42(3), 29 – 33.  
1231 <https://doi.org/10.16765/j.cnki.1673-7148.2019.03.004> (in Chinese)
- 1232 Zheng, L., Sun, J., Zhang, X., & Liu, C. (2013). Organizational modes of mesoscale  
1233 convective systems over Central East China. *Weather and Forecasting*, 28(5),  
1234 1081–1098. <https://doi.org/10.1175/WAF-D-12-00088.1>
- 1235 Zheng, Y., Chen, J., & Zhu, P. (2008). Climatological distribution and diurnal variation  
1236 of mesoscale convective systems over China and its vicinity during summer.  
1237 *Chinese Science Bulletin*, 53(10), 1574–1586.  
1238 <https://doi.org/10.1007/s11434-008-0116-9>
- 1239 Zhu, L., Liu, J., Zhu, A., Sheng, M., & Duan, Z. (2018). Spatial distribution of diurnal  
1240 rainfall variation in summer over China. *Journal of Hydrometeorology*, 19(4), 667–  
1241 678. <https://doi.org/10.1175/JHM-D-17-0176.1>
- 1242 Zipser, E. J. (1977). Mesoscale and convective-scale downdrafts as distinct  
1243 components of squall-line structure. *Monthly Weather Review*, 105(12), 1568–1589.  
1244 [https://doi.org/10.1175/1520-0493\(1977\)105<1568:MACDAD>2.0.CO;2](https://doi.org/10.1175/1520-0493(1977)105<1568:MACDAD>2.0.CO;2)